Bulletin of the Geological Society of Finland, Vol. 92, 2020, pp 39–71, https://doi.org/10.17741/bgsf/92.1.003

Age and origin of the Nb-Zr-REE mineralization in the Paleoproterozoic A1-type granitoids at Otanmäki, central Finland

Kimmo Kärenlampi[1*], Asko Kontinen[2], Eero Hanski[1], Hannu Huhma[3], Yann Lahaye[3], Joachim Krause[4], Thomas Heinig[4]

[1] *Oulu Mining School, P.O. Box 3000, 90014 University of Oulu, Finland*
[2] *Geological Survey of Finland, P.O. Box 1237, 70211 Kuopio, Finland*
[3] *Geological Survey of Finland, P.O. Box 96, 02151 Espoo, Finland*
[4] *Helmholtz Center Dresden—Rossendorf, Helmholtz-Institute Freiberg for Resource Technology, Chemnitzer Str. 40, D-09599 Freiberg, Germany*

Abstract

The Otanmäki area in central Finland hosts two occurrences of Nb-Zr-REE mineralization, Katajakangas and Kontioaho, within a suite of ca. 2.04–2.06 Ga (A1-type) gneissic granites, syenite and monzonite-monzodiorite. They exhibit trace element characteristics and whole-rock ε_{Nd}(2050 Ma) values (from +2.6 to -1.3) consistent with derivation by differentiation of mantle-derived mafic magmas with variable interaction with crustal material. The mineralization is localized in 0.1- to 1.4-m-thick dikes (Katajakangas) and a 30- to 50-m-thick sheet-like body (Kontioaho), containing allanite-(Ce), zircon, titanite, and Nb-REE-Th-U oxides. Their wall rocks are composed of ca. 2.06 Ga peraluminous monzogranite, which is genetically unrelated to the mineralized rock units, as evidenced by whole-rock chemical and Sm-Nd isotope data and zircon U-Pb geochronology. Instead, the mineralization is linked to the nearby peralkaline to metaluminous alkali feldspar granite magmatism dated at ca. 2.04–2.05 Ga. The development of REE-HFSE enrichment in the mineralized rock units required extensive crystallization of a peralkaline granite magma, producing residual metaluminous, high-silica melts enriched in REE-HFSE, Ca, and Fe relative to Na, K, and Al. The REE-HFSE and Ca enrichment was further promoted by volatile complexing with dissolved F^-, CO_3^{2-} and SO_4^{2-}. These highly evolved melts were parental to the mineralized dikes and the sheet-like intrusive body, which were emplaced into the monzogranite capping the intrusions of peralkaline granite.

Keywords: REE mineralization, allanite-(Ce), A1-type granite, geochemistry, U-Pb dating, Sm-Nd isotopes, Paleoproterozoic, Otanmäki

* Corresponding author (e-mail: kimmo.karenlampi@oulu.fi)

Editorial handling: Ferenc Molnàr (e-mail: ferenc.molnar@gtk.fi)

1. Introduction

The rare earth elements (REEs), including the lanthanides and yttrium, are widely used in modern technology, for example, in manufacturing of permanent magnets (Nd, Pr, Sm, Dy), phosphors (Eu, Y, Nd, Tb, Er, Gd), batteries, metal alloys, catalysts, glass, and ceramics (La, Ce, Pr, Nd, Gd, Er, Ho) (e.g., Charalampides et al., 2015). The annual global production of REEs was approximately 210 000 metric tons in 2019 (USGS, 2020). The current production comes mostly from China, USA, Russia, and Australia, where the minable deposits of REEs are associated with carbonatites, alkaline-peralkaline igneous rocks and ion adsorption clays (Weng et al., 2015; Goodenough et al., 2017; USGS, 2020).

In Finland, there are several REE occurrences related to carbonatites, granites, syenites, and hydrothermal alteration zones (Sarapää et al., 2013, 2015; Al-Ani et al., 2018). One of these occurrences is found in the Otanmäki area, central Finland, within a suite of ferroan, A1-type granites and associated intermediate rocks (Kärenlampi et al., 2019). In this area, the first indications of the presence of REE mineralization was obtained in 1981 when radioactive glacial boulders containing high concentrations of REEs and other rare metals, such as Nb and Zr, were found (Äikäs, 1990). The follow-up exploration drilling program between 1983 and 1985 led to the discovery of two Nb-Zr-REE occurrences, which were named Katajakangas and Kontioaho (Hugg & Heiskanen, 1986). According to the preliminary mineral resource estimates from that time, the Katajakangas mineralization contains 0.46 Mt of rock with 2.3 wt.% total REE (TREE), 0.5 wt.% Nb, and 0.8 wt.% Zr (Hugg, 1985a) and the Kontioaho mineralization contains 4 Mt of rock with 0.6 wt.% TREE, 0.08 wt.% Nb, and 2.1 wt.% Zr (Hugg, 1985b). It should be noted, that these estimates are based on sparse drilling information and are noncompliant with modern international reporting standards, such as the JORC Code.

In this paper, we present the first detailed description of the geological setting as well as the geochemical and mineralogical characteristics of the Otanmäki Nb-Zr-REE occurrences together with results of U-Pb and Sm-Nd isotope studies. These data are used to discuss the timing and nature of the mineralizing processes and the source of the rare metals. At present, the Otanmäki REE occurrences are more of geological and mineralogical than economical interest as their Nb-Zr-REE mineral assemblages (allanite-(Ce), zircon, titanite and Nb-REE-Th-U oxides) are unfavorably different from those in the deposits that are currently being mined (e.g., Verbaan et al., 2015; Weng et al., 2015). This is a major challenge for their economic extraction, requiring development of new, economically viable beneficiation technologies.

2. Geologic setting

The Nb-Zr-REE enrichment in the Otanmäki area is associated with a suite of peralkaline to peraluminous granites and intermediate rocks, which belong to the ca. 2.04–2.06 Ga continental rifting-related Otanmäki A1-type suite (Kärenlampi et al., 2019). The geochemical characteristics of these rocks indicate that they originated by differentiation of mantle-derived oceanic island basalt-like melts (Kärenlampi et al., 2019). The Otanmäki suite A1-type plutons were affected by deformation and amphibolite-facies (~550–600 °C and ~4 kbar) metamorphism during the ca. 1.9–1.8 Ga Svecofennian collisional orogeny (Kärenlampi et al., 2019). Consequently, the A1-type rocks display gneissic structures and occur in a 60-km-long, E- to W-trending thrust sheet having faulted boundaries against the surrounding Archean TTG complexes and cratonic platformal and riftogenic supracrustal rocks of the Paleoproterozoic Kainuu belt (Fig. 1a).

The Nb-Zr-REE mineralized rock units are located in the westernmost part of the thrust sheet (Fig. 1a), in which four types of A1-type igneous rocks are recognized: 1) peraluminous monzogran-

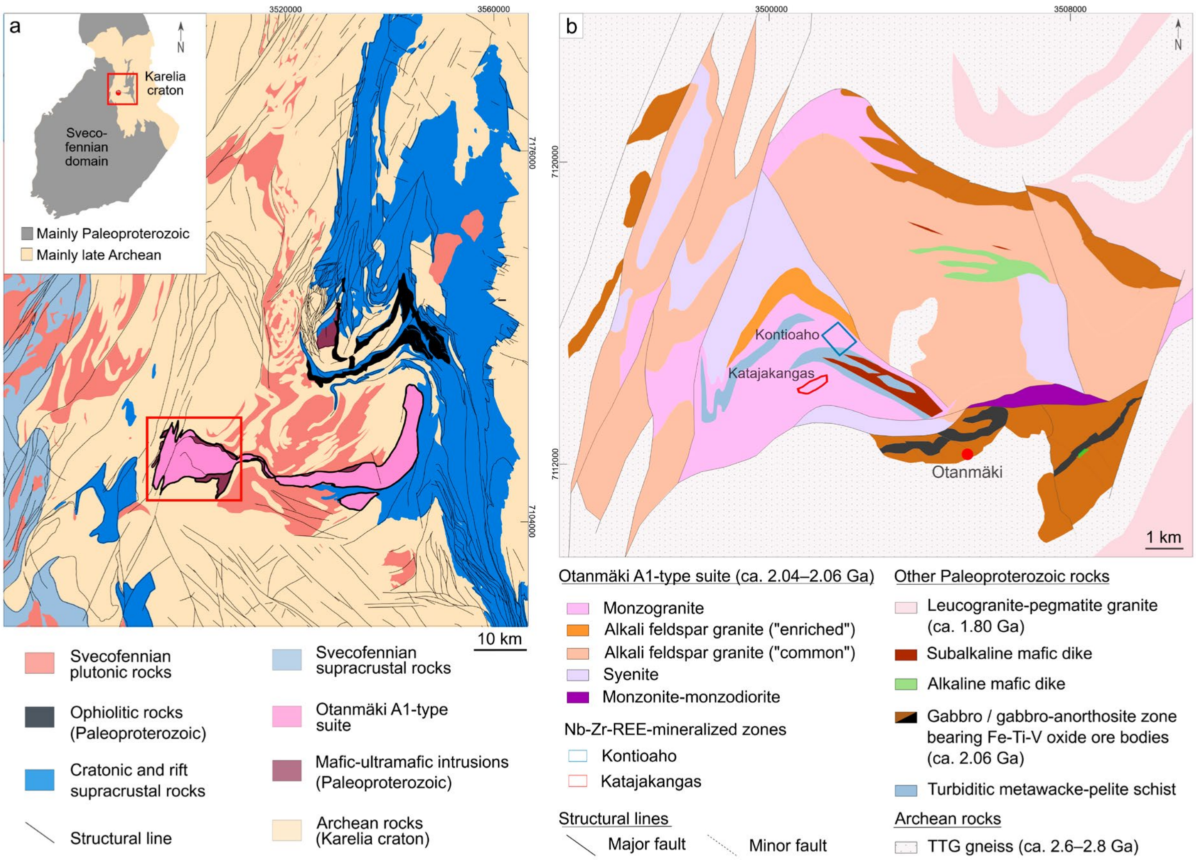

Figure 1. Geology of the Nb-Zr-REE mineralization at Otanmäki. a) Maps showing the geological setting of the Otanmäki suite A1-type felsic to intermediate igneous rocks and the location of the study area (red rectangle) (modified after Bedrock of Finland – DigiKP and Kärenlampi et al., 2019). b) Geological map of the study area showing the location of the Kontioaho and Katajakangas Nb-Zr-REE-mineralized zones. Coordinates in KKJ-3/Finland Uniform Coordinate System.

ite, 2) peralkaline to metaluminous alkali feldspar (AF) granite, 3) syenite, and 4) monzonite–monzodiorite (Fig. 1b). The Nb-Zr-REE occurrences occur within a monzogranite body. Two monzogranite samples have been dated using in-situ LA-SC-ICP-MS analysis, yielding U-Pb zircon ages of 2055 ± 8 Ma and 2060 ± 29 Ma (Kärenlampi et al., 2019). Zircon fractions from two samples of the AF granite have given ages of 2049 Ma ± 10 Ma and 2041 ± 5 Ma (LA-MC-ICP-MS analysis; Kärenlampi et al., 2019). The A1-type rocks are spatially associated with tectonized mafic intrusive bodies, including subalkaline mafic dikes and the Fe-Ti-V oxide ore-bearing Otanmäki gabbro, which has been dated at 2058 ± 15 Ma (Fig. 1b; Huhma et al., 2018). The Otanmäki gabbro is also cut by alkaline mafic dikes having an OIB-like chemical affinity, indicating that they could be genetically linked to the A1-type intermediate-felsic magmatism (see Chapter 6 Geochemistry).

3. Materials and methods

Field work in this study was carried out during 2016–2018, resulting in about 1000 field observations. In addition, 22 diamond drill cores from the Nb-Zr-REE mineralized rock bodies and surrounding bedrock were studied at the Finnish National Drill Core Archive at Loppi. A polarized light microscope with transmitted and reflected light capabilities was used at the University of Oulu to study about 250 polished thin sections, of which 66 represent the Nb-Zr-REE mineralization.

Chemical compositions of Nb-Zr-REE-bearing minerals were determined by wavelength dispersive X-ray spectroscopy (WDS) at the Helmholtz-Institute Freiberg (HIF) with a JEOL JXA-8530F electron probe microanalyzer (EPMA) and *JEOL* JXA-8200 EPMA at the Centre of Material Analysis, University of Oulu. For the description of the quality control procedures and analytical conditions, see Electronic Appendices A and B. In addition, at the HIF, a FEI Quanta 650 F field emission scanning electron microscope (FE-SEM) with two Bruker Quantax X-Flash 5030 energy-dispersive X-ray detectors (EDS) was employed for semi-automated scanning of polished thin sections and FEI's Mineral Liberation Analyzer (MLA) software suite 3.4.1 for data acquisition, processing and evaluation.

Whole-rock major and trace element compositions were determined in two laboratories, the Bureau Veritas Minerals Ltd (Canada) and Labtium Oy (Finland). The analyses at Bureau Veritas were conducted by inductively coupled plasma optical emission spectrometry and mass spectrometry (ICP-OES/-MS) which included sample powder fusion in lithiumborate and dissolution in HNO_3. Total S and C contents were determined using LECO combustion analysis and F by a fluoride-specific electrode. The whole-rock analyses of the samples sent to Labtium Oy were made using X-ray fluorescence (XRF), ICP-OES/ICP-MS, and LECO. For ICP analysis, the samples were digested in HF-$HClO_4$ or HF-$HClO_4$ supplemented with lithium metaborate-sodium perborate fusion (for more details, see Electronic Appendix A). In addition to the analytical data mentioned above, we utilized major and trace element data of 30 samples from Kärenlampi et al. (2019) and the Rock Geochemical Database of Finland (Rasilainen et al., 2007). Furthermore, we had access to unpublished major and trace element data of Rautaruukki Oy mining company, obtained in 1980–1985 with a Philips PW1480 XRF spectrometer and pressed powder pellets. For quality control, several drill core intervals previously analyzed by Rautaruukki Oy were resampled and analyzed at Bureau Veritas or Labtium Oy, with the results indicating a very good correspondence for most of the major and trace elements (see Electronic Appendix C). In addition, we also report previously unpublished major and trace element data of alkaline mafic dike samples from the Otanmäki area obtained using a Siemens SRS 303 XRF spectrometer and pressed powder pellets at the University of Oulu and ICP-MS analysis at the GTK.

Single grain zircon U-Pb isotope analysis was performed using a Cameca IMS 1280 ion probe at the NordSIMS facility, Swedish Museum of Natural History, Stockholm. The primary spot diameter was 10 µm and the general analytical procedure similar to that described by Jeon and Whitehouse (2015) and references therein. The age calculations and concordia diagrams were made using the Isoplot/Ex 4.15 program (Ludwig, 2008).

The first batch of the Sm-Nd whole-rock isotope analyses were made in 1995–2008 at the Geological Survey of Finland (GTK) by isotope dilution thermal ionization mass spectrometry (ID-TIMS) following the procedure described by Huhma et al. (2018). The second batch was made in 2018 at ALS Scandinavia AB, following its standard procedure, which includes digestion of samples by alkali fusion and a $C_4H_6O_6$-HNO_3 mixture, separation of Sm-Nd by ion exchange chromatography, and isotope measurements by inductively coupled plasma-sector field mass spectrometry (for more details, see Electronic Appendix A). The latest batch was made in 2019 at the Finnish Isotope Geoscience Laboratory by high resolution multicollector ICP-MS after sample digestion in a HF-HNO_3 mixture and separation of Sm and Nd by ion exchange chromatography (for more details, see Electronic Appendix A).

4. Geology and petrography of the Otanmäki Nb-Zr-REE occurrences

4.1. Local geology

The Nb-Zr-REE mineralization at Otanmäki consists of two occurrences, Katajakangas and Kontioaho, located approximately 1 km apart (Fig. 2a). The occurrences are within a triangular block (~16 km^2) consisting of fine-grained monzogranite gneiss, which encloses metapsammite-pelite schist slivers up to 200 m in thickness and 5 km in length. The monzogranite and metasedimentary rock units also host foliation-concordant amphibolite sheets (1 to 20 m in thickness), being deformed and metamorphosed subalkaline mafic dikes. Information on the contacts between the monzogranite block and the surrounding A1-type rocks is scarce. At the northern margin of the monzogranite body, a deformed contact against an AF granite has been intersected by several drill holes (Fig. 2a). This contact is interesting with respect to the occurrence of Nb-Zr-REE mineralization, as the flanking AF granite is enriched in incompatible trace elements (e.g., REEs, Zr, Nb, and F) compared to the common AF granite elsewhere in the study area (see Chapter 6 Whole-rock geochemistry). The mineralogical characteristics of the A1-type rocks in the Otanmäki area are summarized in Table 1.

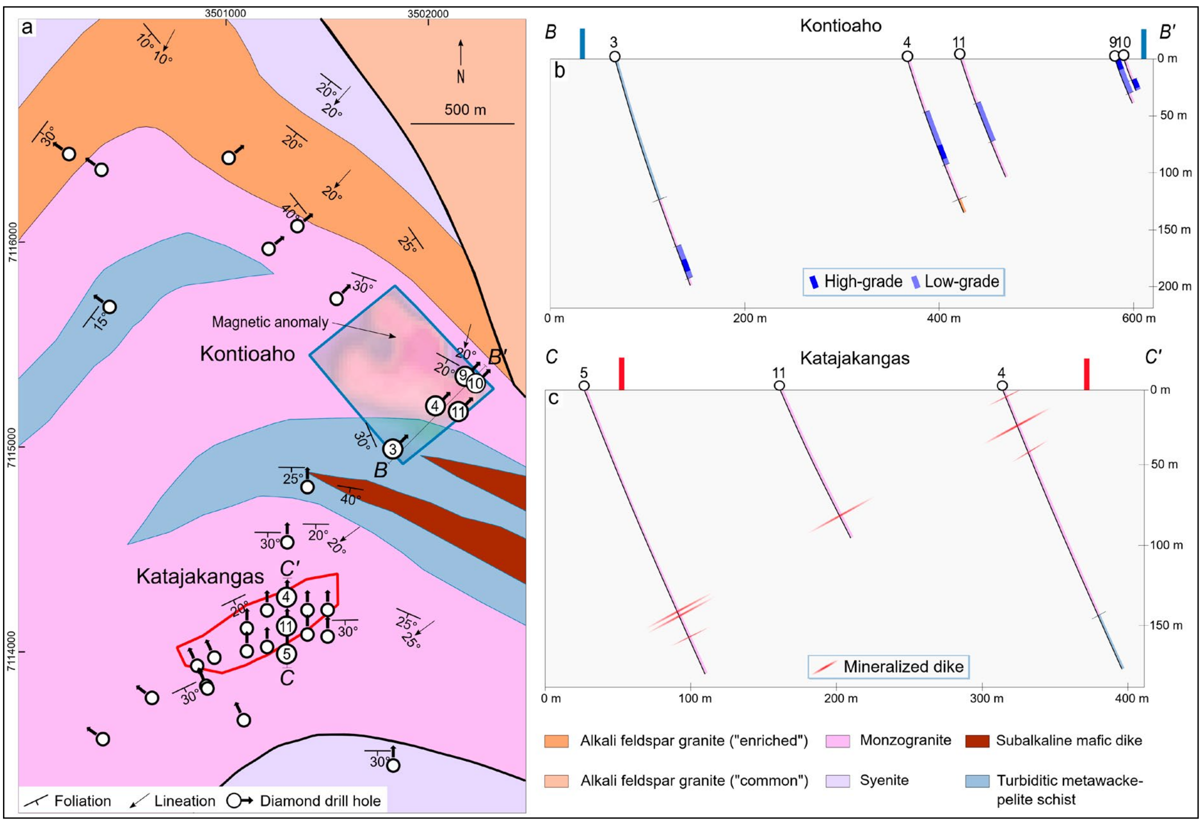

Figure 2. Local geology and occurrences of mineralized zones at Otanmäki. a) Geological map showing the inferred surface projections of the Kontioaho and Katajakangas mineralized zones and diamond drill holes. b–c) Simplified vertical cross-sections of the mineralized rock units. The drilling profiles (B–B', C–C') shown in Fig. 2a. Coordinates in KKJ-3/Finland Uniform Coordinate System.

Table 1. Mineralogical characteristics of barren A1-type igneous rocks in the Otanmäki area.

Rock type	Major minerals	Minor minerals
Monzogranite wall rock	Potassium feldspar, plagioclase, quartz	Biotite, magnetite
Alkali feldspar granite (“enriched”)	Alkali feldspars, quartz	Aegirine, riebeckite, magnetite
Alkali feldspar granite (“common”)	Alkali feldspars, quartz	Aegirine/aegirine-augite, riebeckite/katophorite, (biotite), (aenigmatite), (magnetite)
Syenite	Alkali feldspars	Amphibole, clinopyroxene, (biotite), (magnetite), (quartz)
Monzonite-monzodiorite	Plagioclase, potassium feldspar, biotite, amphibole	Titanite, Fe-Ti oxide, apatite, pyrite

Minerals only occasionally present are indicated by parentheses.

4.2. Kontioaho occurrence

The Kontioaho occurrence consists of a 30- to 50-m-thick, sheet-like body of mineralized rock surrounded by barren monzogranite (Fig. 2b). Its surface exposure is minimal, but on the basis of drill core data, the mineralized body dips 20° to the southwest, extending at least to a depth of 185 m. The drilling-tested strike length of the mineralized body is only 100 m, but based on the magnetic anomaly associated with the magnetite-bearing mineralization, it extends at least 600 m to the NW from the existing drilling profile (Fig. 2a). A magnetic inversion model suggests that the mineralized body reaches a depth of 200–300 m (Lahti et al., 2018).

The observed contacts between the mineralized body and its monzogranite wall rock are sharp and concordant with the foliation in the wall rock, which shows no signs of metasomatic alteration, retaining magmatic-like modal QAP composition and whole-rock chemical compositions. Internally, the mineralized body is divided into high- and low-grade zones, with the former containing >1.5 wt.% Nb+Zr+REE. The high-grade mineralization is confined to a ~12-m-thick zone, usually in the central part of the mineralized body, with the low-grade units being located at its margins (Fig. 2b). The mineralized rocks are pinkish to reddish-grey in color, fine-grained (<1 mm) and banded in texture (Fig. 3). The main minerals are quartz, potassium feldspar, albite, magnetite, zircon, fluorite, allanite-(Ce), and titanite, occurring with small quantities of other minerals (Table 2). The modal QAP composition of the low-grade mineralization is similar to AF granite, which is indicative of a magmatic origin, but the high-grade mineralization is notably depleted in albite relative to potassium feldspar and quartz (Table 2). Allanite-(Ce), zircon, titanite, and Nb-REE-Th-U oxides are located along grain boundaries of quartz and feldspars, form bands or are enclosed in fluorite (Fig. 3).

4.3. Katajakangas occurrence

The Nb-Zr-REE mineralization at Katajakangas consists of single dikes or sets of few (~2–4) dikes ranging from 0.1 to 1.4 m and averaging 0.5 m in thickness. Based on diamond drilling, the dikes are restricted to a tabular zone, which is aligned parallel to the foliation of the host rock, which dips 20–30° to the south (Fig. 2c). The zone has been traced southwards to a depth of 145 m and its NE-SW strike extension is at least 800 m.

The dikes are typically spaced a few meters apart and seem to not cross-cut each other. The dikes have sharp contacts with the monzogranite wall rock. In general, there are no visible signs of chemical reaction in the wall rock, though “metasomatite”

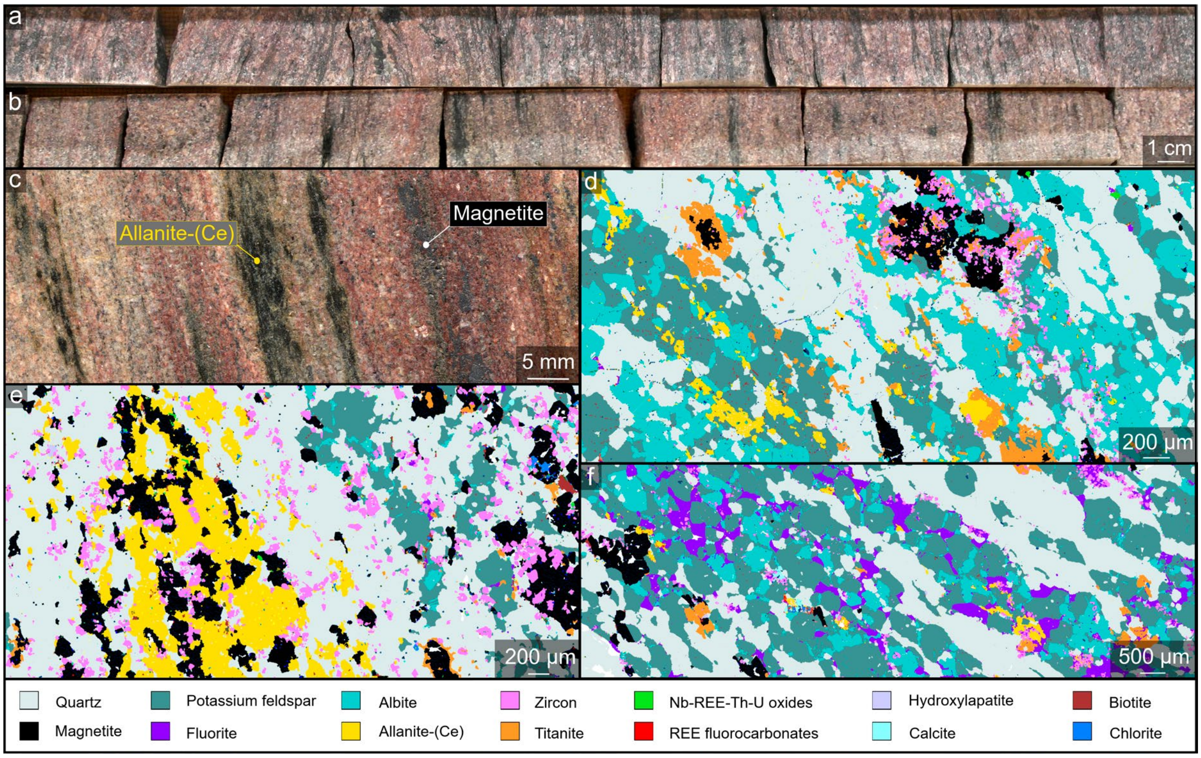

Figure 3. a–b) Photographs of half-split drill core from the Kontioaho mineralization. a) Low-grade zone. b) High-grade zone. c) Polished slab of a high-grade mineralized rock. d–f) FE-SEM scanning-based false color images of polished thin sections representing d) low-grade mineralization, e) high-grade mineralization and f) fluorite-bearing zones in the Kontioaho occurrence.

bands with a thickness of a few tens of centimeters occur locally at the margins of the dikes. These bands are composed of quartz, feldspar, calcite, fluorite, and/or epidote. In the mineralized zone, there are also sets of foliation-concordant calcite veins with a thickness of few mm to cm. Some of these veins contain minor amounts of fluorite. Given the close spatial association of the barren metasomatite bands and calcite±fluorite veins with the mineralized zone, they are likely somehow genetically related to the dikes with Nb, Zr and REE enrichments.

The mineralized dikes are dark grey, very fine grained (<0.5 mm), and foliated (Fig. 4). The main minerals are quartz, allanite-(Ce), albite, zircon, and Nb-REE-Th-U oxides, occurring with small quantities of other minerals, such as calcite, pyrite, and hydroxylapatite (REE-poor) (Fig. 4d; Table 2). Allanite-(Ce), zircon and Nb-REE-Th-U oxides are evenly dispersed in the dikes, occurring as clusters within quartz and albite grains. Quartz represents the dominant gangue mineral (~60 wt.%), being dark and smoky in appearance probably due to irradiation damage induced by the accompanying Th-U-bearing minerals. Quartz is also characterized by extensive, foliation parallel cracks (Fig. 4c), which may have been caused by strain resulting from metamictization-related volume expansion, as such cracks seem to radiate away from the associated Th-U-bearing mineral grains (e.g., allanite-(Ce)). Obviously, the cracks have started to develop only after the high-T (>550 °C) metamorphism in the regime of brittle fracturing of quartz (<300 °C) (cf. Passchier & Trouw, 2005).

Table 2. Minerals found in the Kontioaho and Katajakangas Nb-Zr-REE-mineralized zones together with their structural formulae and abundances (wt.%) in representative samples.

Mineral	Chemical formula	Katajakangas mineralized dikes		Kontioaho, high-grade	Kontioaho, low-grade
Gangue minerals					
Quartz	SiO_2	59.0	61.4	48.0	36.0
Potassium feldspar	$KAlSi_3O_8$	0.4	0.3	25.4	19.5
Albite	$NaAlSi_3O_8$	5.9	6.2	2.3	26.8
Magnetite	Fe_2O_4	*nd*	*nd*	4.6	6.6
Fluorite	CaF_2	*nd*	*nd*	1.9	0.5
Calcite	$CaCO_3$	1.5	3.4	2.1	0.1
Biotite	$K(Mg,Fe)_3(AlSi_3O_{10})(F,OH)_2$	0.7	0.9	0.2	0.4
Chlorite	$(Mg,Fe)_3(Si,Al)_4O_{10}(OH)_2(Mg,Fe)_3(OH)_6$	0.1	0.1	0.3	0.1
Amphibole	$(Na,Ca)_2(Fe^{2+}{}_4Fe^{3+})(Al_2Si_6O_{22})(OH)_2$	0.2	0.2	0.7	0.4
Andradite	$Ca_3Fe_2Si_3O_{12}$	0.2	0.2	0.1	1.2
Hydroxylapatite	$Ca_5(PO_4)_3(F,OH)$	0.5	0.6	0.1	0.2
Pyrite	FeS_2	2.5	2.5	*nd*	*nd*
Nb-Zr-REE-bearing minerals					
Allanite-(Ce)	$(^*Ln,Ca,Y)_2(Al,Fe^{2+,3+})_3(SiO_4)_3(OH)$	19.5	14.7	4.4	2.8
Zircon	$(Zr,Hf,Ln,Y,Nb,U,Th)SiO_4$	2.3	2.5	5.5	2.0
Titanite	$(Ca,Y,Ln)(Nb,Ti,Si)O_5$	0.8	1.2	1.5	1.5
Nb-REE-Th-U oxides		2.8	4.3	0.6	0.3
Fergusonite-(Y)	$(Y,Ln,U,Th)NbO_4$				
Samarskite-(Y)	$(Y,Ln,Fe,U,Th,Ca)(Nb,Ta)_5O_4$				
Euxenite-(Y)	$(Y,Ca,Ln,U,Th)(Nb,Ta,Ti)_2O_6$				
Aeschynite group	$(Y,Ln,Ca,Fe,U,Th)Ti,Nb)_2O_6$				
Pyrochlore group	$(Ca,Na,Y,Ln,U,Th)_2Nb_2O_6(OH,F)$				
Columbite-(Fe)	$Fe^{2+}Nb_2O_6$				
Fersmite	$(Ca,Ln,Na)(Nb,Ta,Ti)_2(O,OH,F)_6$				
REE fluorocarbonates		0.4	0.5	0.6	0.4
Parisite-(Ce)	$Ca(Ln)_2(CO_3)_3F_2$				
Bastnäsite-(Ce)	$(Ln)CO_3F$				

*Ln = lanthanides; nd = not detected.

5. Nb-Zr-REE mineralogy and mineral chemistry

The Nb-Zr-REE mineral assemblages in the mineralized zones at Otanmäki are dominated by silicates and oxides (Table 2). Selected electron microprobe data are presented in Table 3 and all data in Electronic Appendix B. Allanite-(Ce) is the major host for LREEs (La-Sm) and Th in both occurrences. Zircon is the only major host for Zr and a minor host for Th, U, Nb, Y, and HREEs (Gd-Yb). A variety of Nb-REE-Th-U oxide minerals are the major carriers of Nb, Y, HREEs, Th, and U in the Katajakangas dikes, but are less abundant in the Kontioaho mineralization in which titanite is an important carrier of Nb, in addition to being a minor carrier of Y and REEs.

5.1. Allanite-(Ce)

In the Kontioaho mineralized body, allanite-(Ce) forms subhedral to euhedral, tabular crystals (~20–160 μm in length), occurring in disseminations and banded agglomerations together with zircon, magnetite, titanite, and fluorite. In thin sections under transmitted light, allanite-(Ce) grains are turbid and weakly anisotropic and have a dark brown color. In back-scattered electron (BSE) images, the crystals are heterogeneous, displaying growth zoning or irregular variation in brightness

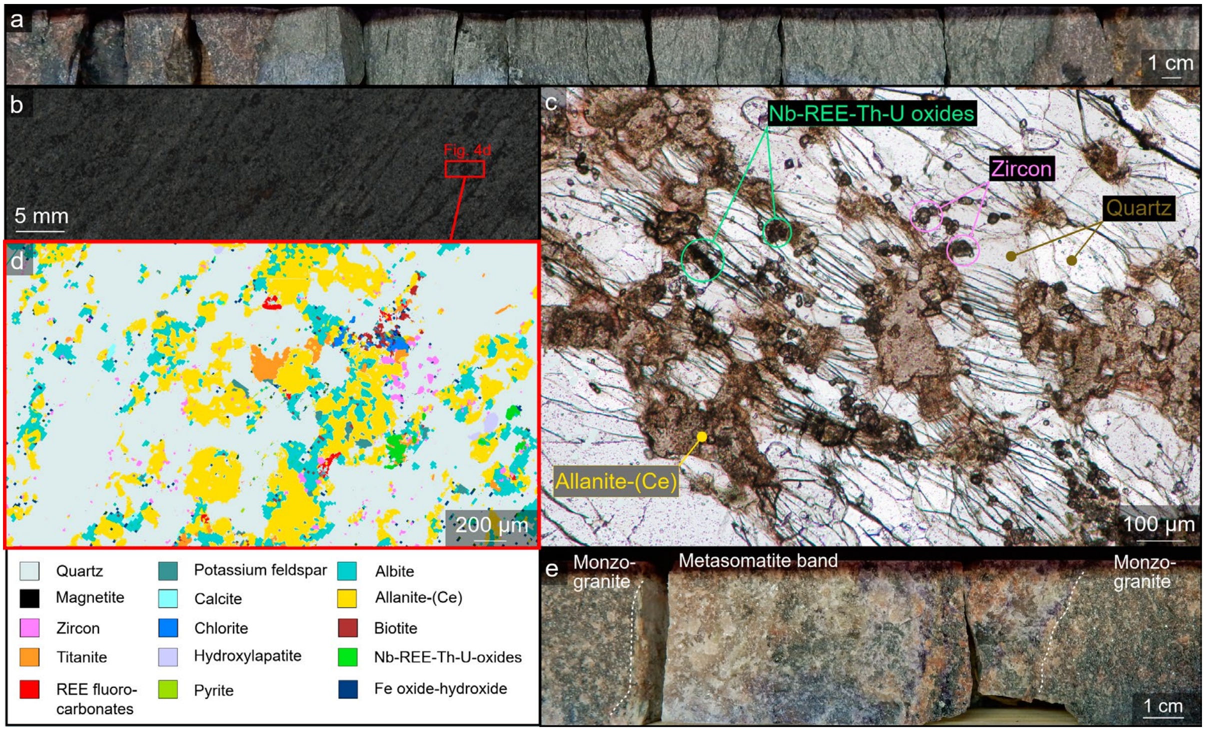

Figure 4. Images of rocks from the Katajakangas mineralization. a) Photograph of a half-split drill core interval showing a 30-cm-thick mineralized dike (dark-grey) in monzogranite wall rock (brownish grey). b) Photograph of a polished slab of a mineralized dike. c) Photomicrograph of a mineralized dike. Transmitted, plane-polarized light. d) FE-SEM scanning-based false-color image of a polished thin section. e) Fluorite-bearing metasomatite band close to a mineralized dike in monzogranite.

(Figs. 5a–b). Allanite-(Ce) crystals are occasionally replaced by minor amounts of acicular REE fluorocarbonate, mostly parisite-(Ce), which appears to be a phase related to metamorphism because its occurrence is restricted to the precursor allanite-(Ce) crystals.

In cross-polarized light, allanite-(Ce) in the mineralized dike-like structures at Katajakangas has a turbid, metamict appearance and in BSE images, it shows irregular bright- and dark patches (Figs. 6a–c). The diameters of allanite-(Ce) grains reach up to 250 µm, but the irregular grain boundaries make it difficult to visually recognize individual crystals. The allanite-(Ce) grains occur in loosely interconnected clusters, in which they occur with albite, zircon, Nb-REE-Th-U oxides, calcite, hydroxylapatite, and/or (rare) REE fluorocarbonates. Cracks in quartz crystals surrounding allanite-(Ce) grains are occasionally filled with a LREE-rich material, mainly REE fluorocarbonate. These LREE-rich fillings appear to be sourced from nearby allanite-(Ce) grains, as they show REE-depleted patches appearing dark in BSE images (Fig. 6c).

The analyzed allanite-(Ce) grains show strong enrichment in LREE over HREE (Table 2) and are thus Ce-dominant, ranging stoichiometrically from ferriallanite to allanite (Fig. 7a). The total REE content varies between 5.9 and 21.5 wt.% and increases with decreasing Ca (2.0–13.0 wt.%), indicating mutual substitution. More generally, the observed compositional variation in allanite compositions suggest that several substitution mechanisms are present for REE^{3+}: $Ca^{2+} + Si^{4+} = REE^{3+} + Al^{3+}$; $REE^{3+} + Fe^{2+} = Ca^{2+} + Fe^{3+}$; $REE^{3+} + Fe^{2+} = Ca^{2+} + Al^{3+}$; $REE^{3+} + Mg^{+} (Mn^{2+}) = Ca^{2+} + Fe^{3+} (Al^{3+})$ (cf. Dollase, 1971; Petrik et al., 1995; Gieré & Sorensen, 2004). The Th content ranges

Table 3. Representative chemical compositions (wt.%) of Nb-Zr-REE-bearing minerals from the Kontioaho and Katajakangas mineralization.

	Kontioaho				Katajakangas				
Mineral	Allanite-(Ce)	Zircon (porous)	Titanite	Samarskite-(Y)	Allanite-(Ce)	Zircon (porous)	Titanite	Fergusonite-(Y)	Euxenite-(Y)
SiO_2	32.15	32.66	29.57	5.47	32.28	32.30	30.41	0.62	*0.07*
TiO_2	0.11	0.20	26.64	2.00	0.20	*bdl*	28.29	0.05	*14.20*
Al_2O_3	14.54	0.03	2.32	0.36	18.09	0.11	5.14	0.04	*bdl*
FeO_{tot}	17.35	0.39	5.46	3.76	9.88	0.37	1.15	2.28	*2.00*
MnO	0.20	0.02	0.05	0.29	0.87	0.15	0.17	0.33	*0.43*
MgO	0.53	0.05	*bdl*	*bdl*	0.47	0.02	*bdl*	*bdl*	*bdl*
CaO	13.71	0.06	24.95	2.69	11.01	0.68	26.09	3.46	*3.90*
Na_2O	*bdl*	0.04	*bdl*	*bdl*	0.04	0.25	*bdl*	0.03	*0.04*
K_2O	0.07	0.09	*bdl*	0.12	0.09	0.13	*bdl*	0.09	*0.11*
P_2O_5	*bdl*	0.09	0.03	0.04	*bdl*	0.18	0.03	0.07	*0.05*
Y_2O_3	0.43	1.93	1.88	11.60	0.05	0.61	0.48	25.75	*14.21*
La_2O_3	3.79	0.05	*bdl*	0.98	4.44	0.06	0.05	0.03	*0.04*
Ce_2O_3	7.82	0.06	0.20	4.70	10.35	0.12	0.35	0.20	*0.63*
Pr_2O_3	0.87	0.04	0.05	0.79	1.17	0.00	0.08	0.07	*0.21*
Nd_2O_3	3.57	0.04	0.25	4.27	4.11	0.05	0.31	0.29	*2.82*
Sm_2O_3	0.30	0.04	0.13	1.55	0.16	0.03	0.10	0.13	*1.88*
Gd_2O_3	0.51	0.18	0.36	2.64	0.33	*bdl*	0.15	2.80	*3.68*
Dy_2O_3	0.12	0.23	0.30	2.52	*bdl*	0.04	0.05	3.92	*2.66*
Er_2O_3	0.03	0.27	0.17	1.38	0.01	0.05	0.02	2.56	*1.23*
Yb_2O_3	0.01	0.36	0.16	0.86	*bdl*	0.17	*bdl*	1.67	*0.73*
ZrO_2	*bdl*	61.85	0.06	0.09	*bdl*	63.28	*bdl*	0.28	*bdl*
HfO_2	*bdl*	1.33	*bdl*	0.07	*bdl*	1.07	*bdl*	0.08	*bdl*
Nb_2O_5	*bdl*	0.38	2.80	45.25	*bdl*	0.11	2.38	44.14	*38.58*
Ta_2O_5	*bdl*	*bdl*	0.33	4.74	*bdl*	*bdl*	1.22	0.76	*2.45*
ThO_2	0.09	0.03	0.01	0.53	0.51	0.15	*bdl*	0.43	*4.05*
UO_2	*bdl*	0.02	*bdl*	0.62	*bdl*	0.19	*bdl*	2.17	*0.91*
F	*bdl*	0.22	1.32	0.15	*bdl*	*bdl*	1.29	0.53	*bdl*
***Total**	96.18	100.34	95.16	97.26	94.05	100.12	95.92	92.01	*94.89*
TREO	17.44	3.19	3.50	31.30	20.62	1.13	1.59	37.41	*28.09*

*The low totals may reflect the presence of water in the crystalline structure and/or metamictization in the Th-U-bearing minerals. *bdl* = below detection limit; TREO = total rare earth oxide.

from several hundreds to few thousands of ppm, whereas in most allanite-(Ce) grains, U was not detected. The varying brightness in BSE images is linked to variations in the REE and/or Th contents, so that the brightest areas are enriched in Th (cores of crystals) and the darkest areas are depleted in REEs relative to other parts of the same crystal (Figs. 5a–b and 6b–c). The analytical totals (~87–96 total oxide wt.%) are lowest in the high-Th domains, possibly indicating a high degree of metamictization and/or hydration in such domains (cf. Gieré & Sorensen, 2004).

5.2. Zircon

Zircon in the Otanmäki Nb-Zr-REE mineralization occurs as disseminated grains, in clusters of a few grains at the boundaries of allanite-(Ce), titanite or Nb-REE-Th-U oxide grains, or as small inclusions in fluorite, allanite-(Ce) or magnetite (Figs. 3 and 4). The zircon crystals are equidimensional, subhedral to anhedral, ranging from 5 to 250 μm and averaging 50 to 90 μm in size. They host abundant micrometer-sized pores and bright Th-U-rich micro-inclusions and show variable trace element (REE, Nb, Th and U) con-

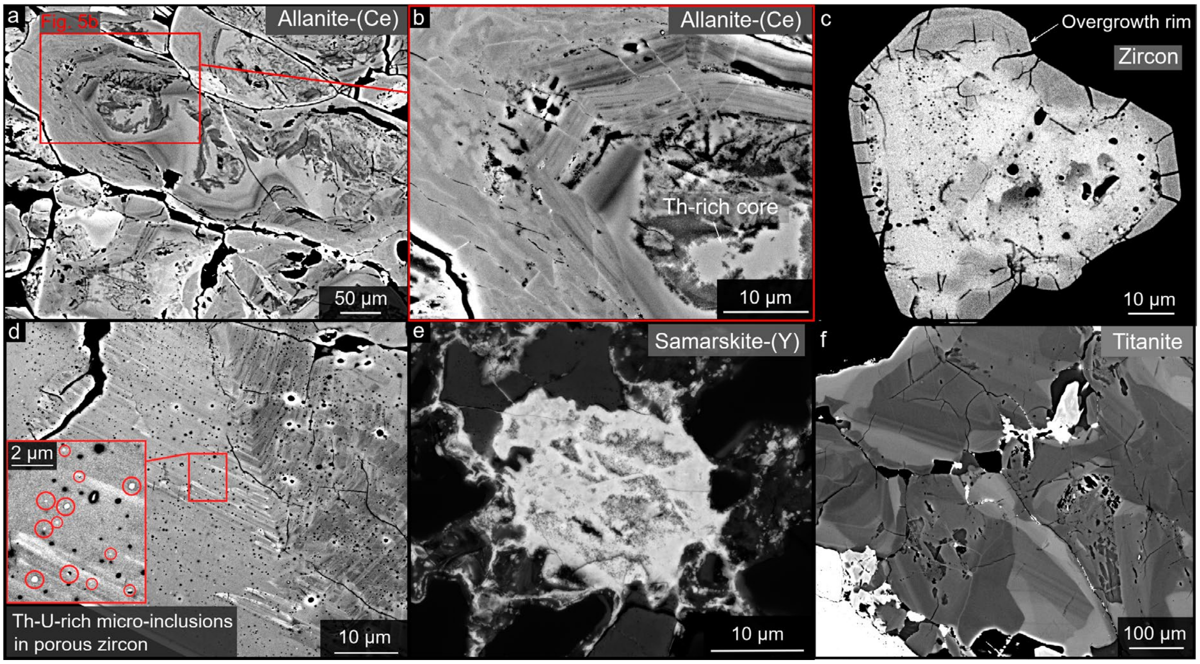

Figure 5. Back-scattered electron images illustrating typical textures of Nb-Zr-REE-bearing minerals in the Kontioaho mineralized zone. a–b) Allanite-(Ce) grains showing varying brightness, growth zoning and Th-rich cores. c) Porous zircon with varying brightness, micrometer-sized pores and overgrowth rims. d) Porous zircon with remnants of oscillatory zoning and Th-U-rich micro-inclusions. e) Samarskite-(Y) grain with a secondary decomposition texture and associated redistribution of REEs and Nb into adjacent cracks and grain boundaries. i) Titanite grains showing a patchwork of brighter and darker domains.

centrations, reflected by brightness differences in BSE images (Figs. 5c–d and 6d–e). Occasionally, the porous zircon grains show remnants of oscillatory growth zoning (Fig. 5d) and commonly, they have overgrowth rims, which lack zoning, porosity and inclusions, appearing darker in BSE images (Figs. 5c and 6d).

The porous zircon domains are characterized by elevated total REE contents (1.0–3.0 wt.%), which are coupled with enrichment in Nb (0.04–1.3 wt.%) and depletion in Zr (44.0–49.8 wt.%.), indicating that the substitution mechanism $REE^{3+} + Nb^{5+} = 2\ Zr^{4+}$ is important (Fig. 7b; cf. Hoskin & Schaltegger, 2003). The dark BSE patches in the analyzed porous zircon grains contain only half of the REE and Nb content of the bright areas and have mostly lower but also more variable Th/U ratios. The overgrowths also show very low REE and Nb contents (Fig. 7b) and Th/U ratios. The Th and U contents of the porous domains are very high, varying from several hundreds to few thousands of ppm (Table 3), even though Th-U-rich inclusions were avoided during the analyses.

5.3. Titanite

Titanite grains appear optically homogeneous and vary in size from 40 to 360 µm. The grains are mostly roundish and anhedral, obviously due to effects of metamorphic recrystallization. Titanite is typically scattered throughout the mineralized rocks, occurring as solitary grains or clusters of small grains devoid of other Nb-Zr-REE-bearing minerals or as agglomerations with allanite-(Ce), zircon, and/or magnetite (Figs. 5 and 6). In BSE images, the titanite grains show either homogeneous internal textures or a complicated patchwork of bright and dark-colored domains (Fig. 5f).

The analyzed titanite grains show highly variable Nb (0.1–3.9 wt.%) and total REE (0.6–4.2 wt.%)

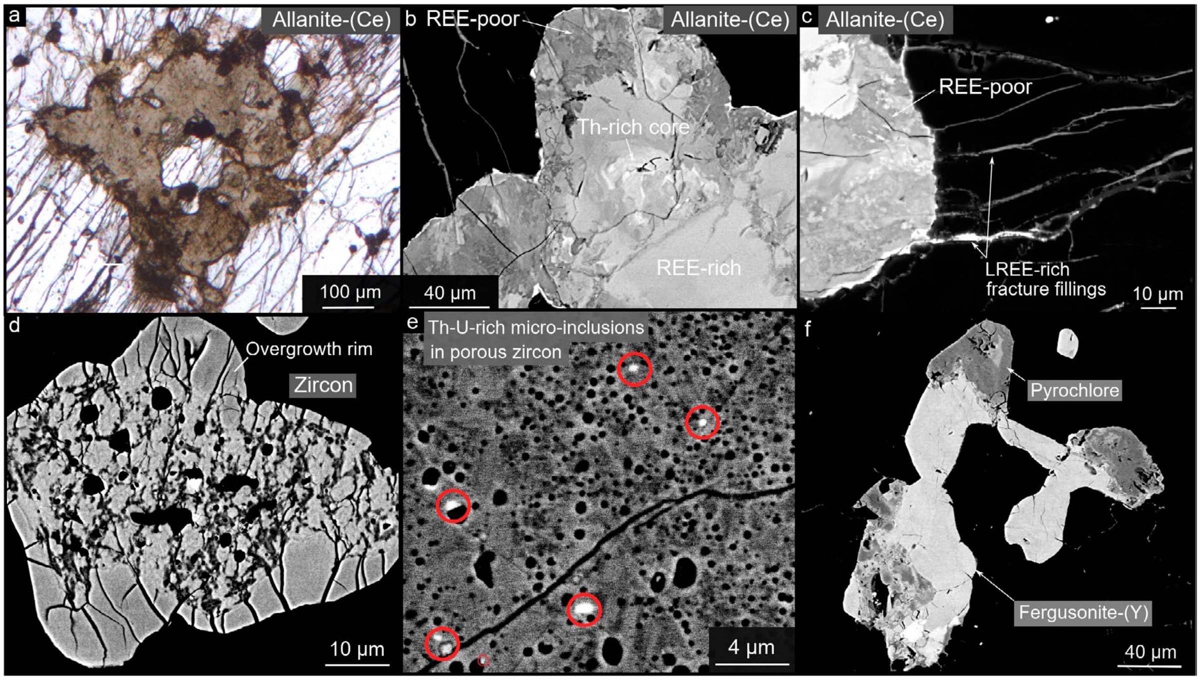

Figure 6. Typical textures of Nb-Zr-REE-bearing minerals in the Katajakangas mineralized dikes. a) Photomicrograph of allanite-(Ce) grain with a turbid, metamict appearance. Transmitted, plane-polarized light. b–f) Back-scattered electron images. b–c) Allanite-(Ce) grains with Th-rich cores and REE-depleted dark patches, and LREE-rich fillings in cracks of surrounding quartz. d–e) Porous zircon grains showing overgrowth rims, micrometer-sized pores and Th-U-rich micro-inclusions. f) Fergusonite-(Y) showing altered parts with a composition similar to that of pyrochlore.

contents, which correlate poorly with each other. The observed negative correlation between Ca and REE indicates that the substitution reaction $Ca^{2+} + Ti^{4+} = REE^{3+} + (Al, Fe)^{3+}$ (Vuorinen & Hålenius, 2005) is important, but because no correlation is observed between Ca and Ti, the substitution scheme has to be more complicated. The titanite grains show elevated F contents (0.5–2.3 wt.%), which indicate a F-rich environment during their crystallization. Negative correlation between Ti and Al + Fe and positive correlation between F and Al + Fe suggest that the substitution mechanism $Ti^{4+} + O^{2-} = (Al, Fe)^{3+} + (F, OH)^{-}$ is important (cf. Bernau & Franz, 1987; Carswell et al., 1996; Pan et al., 2018). Furthermore, the REEs and Fe correlate positively with Al/Fe, suggesting that the replacement of Ca and Ti by REE^{3+} and Fe^{3+} is more important than by REE^{3+} and Al^{3+}. Titanite is likely of magmatic origin as magmatic titanite is characteristically high in REE^{3+} and Fe^{3+} relative to Al^{3+} (Aleinikoff et al., 2002; Pan et al., 2018). However, the observed variation in the Al/Fe ratio in the analyzed titanite grains from 1.0 to 5.2 covers the typical values in both metamorphic (~4) and magmatic (~1–2) titanite (Fig. 7c), suggesting re-equilibration of primary (magmatic) titanite. The Nb substitution scheme is also complex, with two mechanisms being consistent with the compositional data: $Ti^{4+} = Nb^{5+} + Al^{3+} + Fe^{3+}$ (cf. Vuorinen & Hålenius, 2005) and $Ti^{4+} + Si^{4+} = Nb^{5+} + Al^{3+}$ (cf. Černý & Ercit, 1989). The concentrations of Th, U and Zr are close to or below the detection limits.

5.4. Nb-REE-Th-U oxide minerals

Minor amounts of several Nb-REE-Th-U oxide minerals are found in the mineralized rocks, usually as tiny (~5–60 µm across), anhedral, disseminated crystals or as small aggregates of such crystals

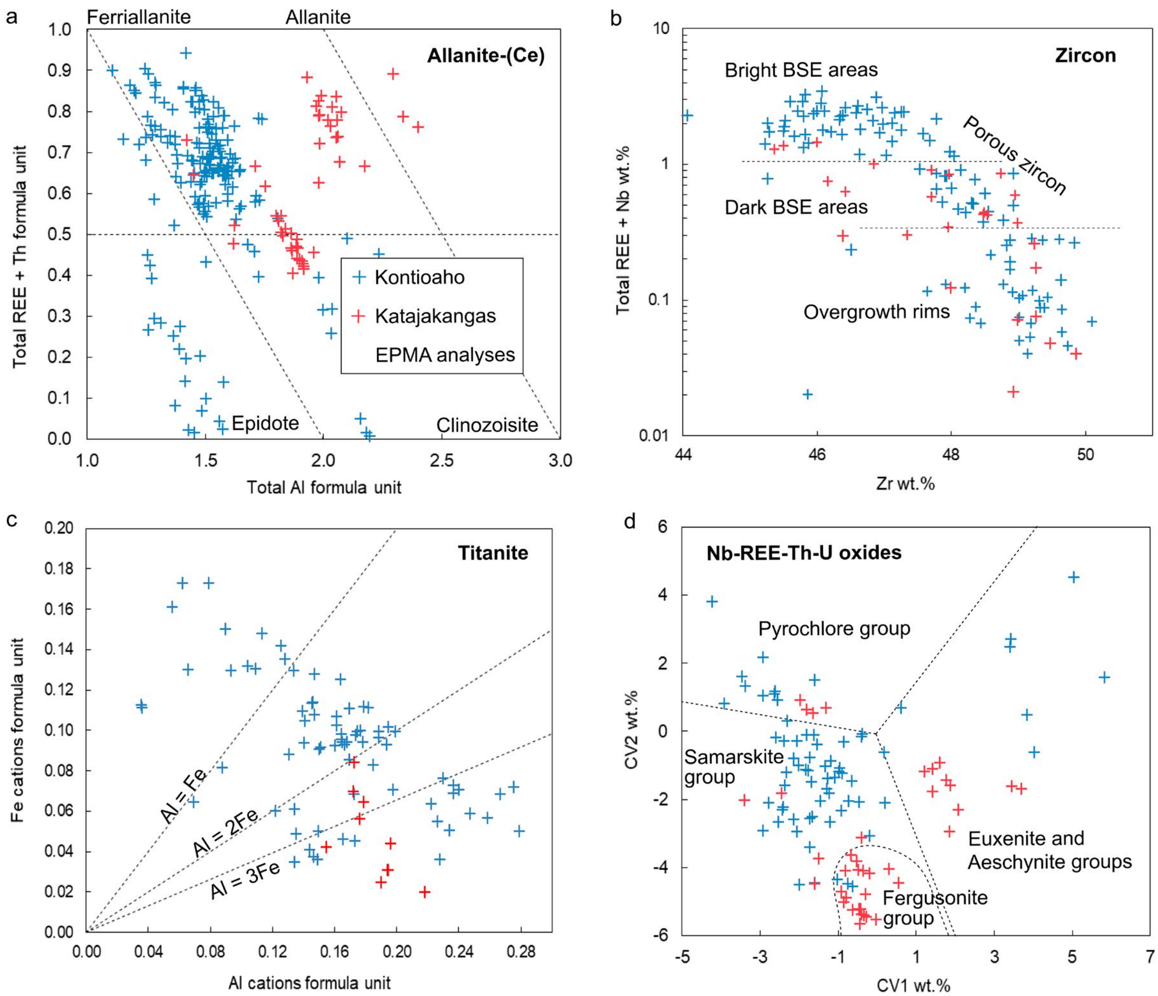

Figure 7. Chemical characteristics of Nb-Zr-REE-bearing minerals in the Kontioaho and Katajakangas mineralization. a) REE+Th vs. Al (cations per formula unit) diagram for the system allanite-ferriallanite-epidote-clinozoisite (Petrik et al., 1995; Gieré & Sorensen, 2004). b) Total REE + Nb vs. Zr diagram for zircon. c) Fe vs. Al cationic diagram for titanite. d) CV2 vs. CV1 diagram after Ercit (2005) for Nb-REE-Th-U oxides. Variables CV1 and CV2 in d) are calculated according to the three-group rule of Ercit (2005) (CV1 = 0.245 Na + 0.106 Ca - 0.077 Fe*(Fe* = Fe + Mn) + 0.425 Pb + 0.220 Y + 0.280 LREE + 0.137 HREE + 0.100 U*(U* = Th + U) + 0.304 Ti + 0.097 Nb + 0.109 Ta*(Ta* = Ta + W) – 12.81 (oxide wt.%), CV2 = 0.102 Na - 0.113 Ca - 0.371 Fe* - 0.167 Pb - 0.395 Y- 0.280 LREE - 0.265 HREE - 0.182 U*- 0.085 Ti - 0. 166 Nb - 0.146 Ta* + 17.29 (oxide wt.%)). Note that only the measured REE (La, Ce, Pr, Nd, Sm, Gd, Dy, Er, Yb, Y) are included in total REE.

(Figs. 5e and 6f). Most of these oxides display altered parts (Fig. 6f) or secondary alteration/decomposition textures, which imply redistribution of REE and Nb into adjacent cracks or along grain boundaries of surrounding minerals (Fig. 5e). The analytical totals for most of the WDS analyses of the Nb-REE-Th-U oxides are low (~86–95 total oxide wt.%), which indicates the presence of water in their crystal structure and/or that these minerals are metamict (cf. Ercit, 2005; Atencio et al., 2010).

The Nb-REE-Th-U oxides have variable contents of total REE (0.7–32.2 wt.%), Nb (3.7–52.2 wt.%), Th (up to 7.9 wt.%), U (up to 7.0 wt.%) and Ta, Ca, Fe, Ti and Si. Using the (Y,REE,U,Th)–(Nb,Ta,Ti) oxide mineral classification diagram of Ercit (2005) (Fig. 7d), the

Table 4. Representative whole-rock analyses from the Kontioaho and Katajakangas mineralization and associated barren (A1-type) igneous rocks (major elements in wt.%, trace elements in ppm).

	Mineralized rock units						Barren A1-type rocks						
Rock type	Katajakangas mineralization		Kontioaho mineralization		Alkali feldspar granite "enriched"		Alkali feldspar granite "common"		Syenite		Monzonite-monzodiorite		Monzo-granite wall rock
SiO_2	70.2	71.3	69.4	72	68.7	71.0	71.0	70.9	60.2	63.6	55.6	47.8	69.2
TiO_2	0.48	0.54	0.67	0.28	0.29	0.44	0.38	0.39	0.75	0.58	1.26	2.61	0.88
Al_2O_3	6.98	7.06	6.3	9.18	9.56	9.68	11.86	12.8	16.7	14.72	16.83	16.12	12.86
FeO_{tot}	4.56	3.24	7.17	6.51	7.14	7.7	4.82	4.23	7.13	6.84	8.98	12.28	4.95
MnO	0.17	0.18	0.04	0.07	0.07	0.06	0.15	0.12	0.22	0.16	0.25	0.24	0.16
MgO	0.16	0.26	0.31	0.19	0.37	0.23	0.07	0.09	0.58	0.06	1.26	2.26	0.85
CaO	4.4	4.72	3.59	2.1	3.15	1.47	0.85	0.64	2.4	1.31	4.32	8.07	1.41
Na_2O	1.06	1.52	0.62	2.8	2.64	3.96	4.52	4.87	6.19	6.46	5.8	4.7	2.43
K_2O	0.23	1.94	4.36	3.96	4.44	3.23	5.41	4.99	4.83	5.17	3.47	1.74	5
P_2O_5	0.2	0.19	0.02	0.06	0.01	<0.01	0.03	0.03	0.26	0.03	0.57	1.41	0.19
F	0.04	0.06	1.48	0.73	0.62	0.48	*nd*	0.08	*nd*	0.27	*nd*	0.11	0.1
CO_2	0.62	2.89	0.07	0.51	1.43	0.15	*nd*	0.1	0.23	*nd*	*nd*	*nd*	0.37
S	<0.02	1.04	<0.02	<0.02	<0.02	<0.02	*nd*	*nd*	0.04	<0.02	0.02	0.07	0
Cl	*nd*	*nd*	*nd*	*nd*	*nd*	*nd*	*nd*	*nd*	0	*nd*	0.01	*nd*	*nd*
LOI	3.2	4.3	1.3	0.9	2.1	*nd*	0.44	*nd*	*nd*	0.2	*nd*	0.9	*nd*
Total	92.33	99.24	95.38	99.26	100.5	98.4	99.52	99.22	99.54	99.38	98.33	98.29	98.39
Co	*nd*	*nd*	*nd*	*nd*	*nd*	*nd*	*nd*	0.8	3.6	*nd*	8.4	*nd*	*nd*
V	<8	<8	<8	<8	<8	9	14	1.1	<5	<8	<5	33	29
Sc	17	5	<1	2	<1	<1	*nd*	0.9	4.7	<1	7.1	13	7
Nb	8821	4451	748	792	501	321	215	54	55	49	44	9	41
Ta	421	237	86	48	28	27	17	2.8	2.5	2.2	2.2	0.5	2.3
Zr	11270	7451	33310	4423	1575	1604	980	197	102	194	89	68	339
Hf	216	135	835	111	42	50	30	4.4	4.1	4.8	3.5	1.6	8.8
Ba	144	317	74	57	49	26	170	229	870	98	5956	2832	2208
Sr	396	264	52	50	38	16	25	23	96	11	714	823	107
Rb	15	98	428	420	373	250	260	124	99	111	55	21	165
Th	1928	1133	67	210	89	39	38	7.1	4.7	7.6	5	1.3	17
U	578	237	73	36	19	10	5.8	1.7	0.5	1.3	0.51	0.3	5
Ga	45	22	33	47	40	40	34	37	27	36	16	18	25
Sn	227	98	60	35	13	23	*nd*	*nd*	<30	2	*nd*	*nd*	3
Y	2616	2219	763	384	250	115	120	24	17	25	21	15	32
La	7075	3581	1038	776	394	219	170	52	32	70	41	18	60
Ce	15639	8164	2029	1358	773	395	330	108	68	131	83	44	118
Pr	1852	895	236	157	93	44	38	13	8.5	15	10	6.6	14
Nd	6741	3250	922	566	337	156	140	50	34	53	42	33	53
Sm	1314	605	183	99	64	27	28	8.5	5.9	8.5	7.5	6.7	9.9
Eu	124	60	21	11	7.8	3.2	4.2	1.2	2.2	1.2	5.5	4.6	2.4
Gd	1113	512	147	83	58	25	34	7.3	5	6.8	6.5	6.3	8.2
Tb	156	81	24	12	9.0	4	5.2	1	0.7	0.9	0.8	0.8	1.1
Dy	754	446	144	70	51	24	26	4.7	3.7	5.2	4.5	3.7	6.4
Ho	120	85	31	14	9.9	4.9	4.9	0.9	0.7	1	0.8	0.6	1.2
Er	286	219	101	40	28	14	15	2.6	1.8	2.8	2.1	1.4	3.3
Tm	36	27	17	5.7	3.7	1.9	2	0.4	0.3	0.4	0.3	0.2	0.4
Yb	205	144	133	34	22	12	12	2.7	1.8	3.1	1.6	1.1	2.7
Lu	25	17	22	4.6	3.0	1.8	1.7	0.4	0.3	0.6	0.3	0.2	0.4
TREE	38056	20305	5811	3614	2103	1047	931	277	182	325	227	142	313
Al/(Na+K) molar	3.50	1.54	1.10	1.03	1.05	0.97	0.89	0.95	1.08	0.91	1.27	1.68	1.37
Al/(Ca+Na+K) molar	1.17	0.79	0.70	0.85	0.80	0.85	0.84	0.91	0.95	0.85	0.98	0.95	1.20
$FeO_{tot}/(FeO_{tot} + MgO)$	0.97	0.93	0.96	0.97	0.95	0.97	0.99	0.98	0.92	0.99	0.88	0.84	0.85

nd = not determined, LOI = loss of ignition, TREE = total rare earth elements.

dominant Nb-REE-Th-U oxides are fergusonite, aeschynite-euxenite, and samarskite group minerals, more specifically fergusonite-(Y), euxenite-(Y), and samarskite-(Y) (Table 2). These minerals show altered parts that are compositionally similar to samarskite, aeschynite-euxenite, or pyrochlore group minerals. In a small number of the Nb-rich oxide grains, the compositions are similar to those of columbite-(Fe) or fersmite.

6. Whole-rock geochemistry

In total, we report 107 whole-rock analyses from Kontioaho and 66 from Katajakangas. In addition, we analyzed samples from barren A1-type rocks surrounding the Nb-Zr-REE occurrences. A representative set of whole-rock compositions is listed in Table 4 and all data in Electronic Appendix C.

6.1. Barren A1-type rocks

The barren A1-type rocks exhibit a wide range of SiO_2 contents varying from ~48 wt.% in monzonites-monzodiorite, via ~63 wt.% in syenite to ~76 wt.% in the granites (AF granite, monzogranite). In the TAS diagram (Fig. 8a), the trend of the intermediate rocks extends from monzogabbro via monzonite to syenite, while the granites plot dominantly in the field of granite. The monzogranite samples are peraluminous, but the AF granite shows variable alkalinity, as samples of the common type are peralkaline, whereas samples of the enriched type are transitional between peralkaline and metaluminous (Fig. 8b). The intermediate rocks are mostly metaluminous (Fig. 8b). The barren A1-type rocks all show a ferroan composition with high Fe/Mg ratios (FeO_{tot}/(FeO_{tot} + MgO) = ~0.8–1.0; Table 4).

In primitive mantle-normalized multi-element diagrams, the monzogranite and AF granite share many features including strong depletion in Ba, Sr, P, and Ti, enrichment in Zr-Hf relative to REEs (expect Eu), and negative Eu anomalies (Eu/Eu* = ~0.3–0.5 for AF granite and ~0.6–0.8 for monzogranite) (Figs. 9a–b). The spidergram patterns also reveal that compared to the AF granite, the monzogranite samples have lower levels of Nb-Ta relative to Th-U and Zr-Hf, which may be an indication of a greater amount of material input

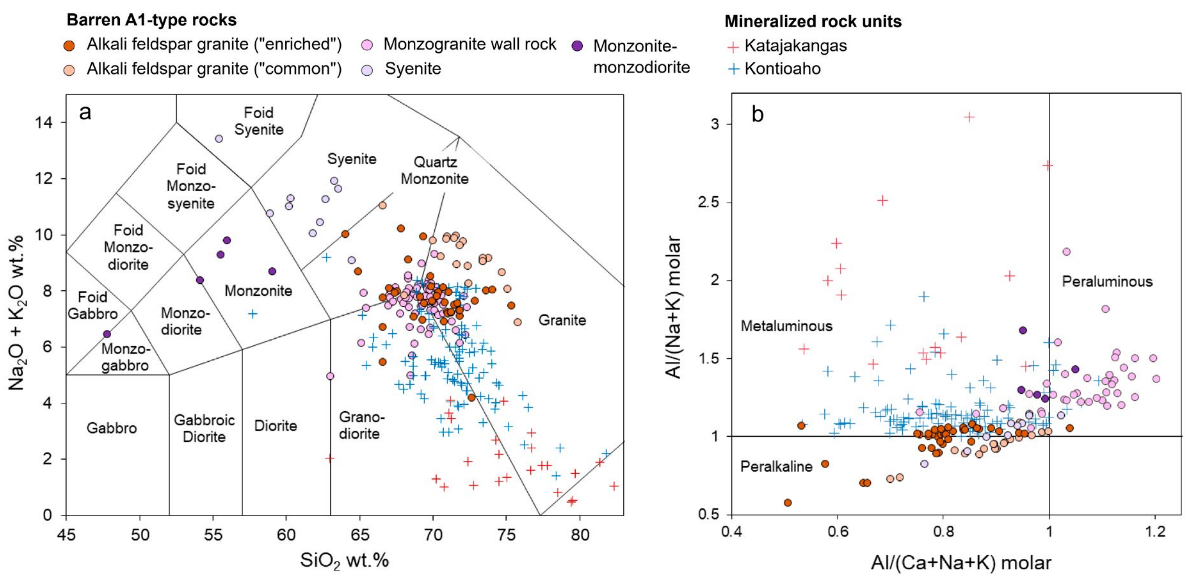

Figure 8. Major element data of mineralized samples from Kontioaho and Katajakangas and associated barren A1-type rocks from the Otanmäki area. a) Total alkalis vs. SiO_2 diagram (Middlemost, 1994). b) Molar Al/(Na+K) vs. Al/(Ca+Na+K) diagram (Shand, 1943).

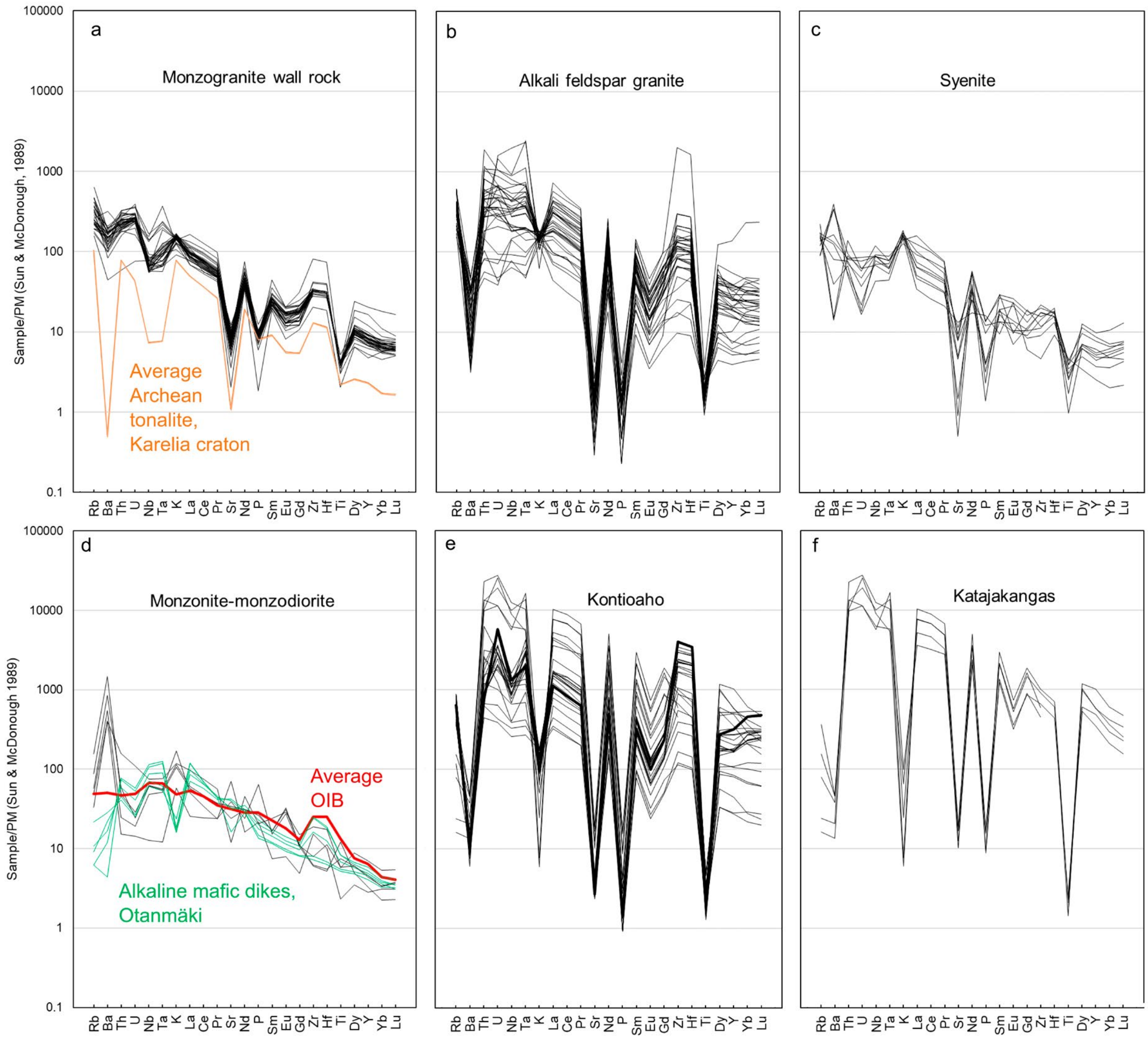

Figure 9. Primitive mantle-normalized multi-element spidergrams for samples from the a–d) Otanmäki suite barren A1-type rocks and alkaline mafic dikes from the Otanmäki area and e) Kontioaho and f) Katajakangas mineralized rock units. For comparison an average composition of OIB (oceanic island basalt; Sun & McDonough, 1989) and Archean tonalite from the Karelia craton (Rasilainen et al., 2007) are also shown in a) and d). Normalization values from Sun and McDonough (1989).

from crustal sources in the genesis of monzogranite. The monzogranite and, to a lesser extent, the AF granite show incompatible trace element ratios, such as Nb/U and Th/Yb (Fig. 10a), that are closer to those of the average upper continental crust and Archean TTGs from the Karelia craton than those of average OIB or alkaline mafic dikes and intermediate A1-type rocks in the Otanmäki area, thus suggesting involvement of crustal contamination in the generation of granite. The AF granite is also distinct from the other A1-type rocks in the Otanmäki area because it exhibits the highest Zr/Ti fractionation and total REE contents (Fig. 10b), which are likely results from significantly higher degrees of fractionation in its parent magma. The syenite samples show a roughly similar trace element signature to that of the granite samples, with the exception that they show less pronounced Ti and P depletions, conspicuous positive K anomalies and a division into either

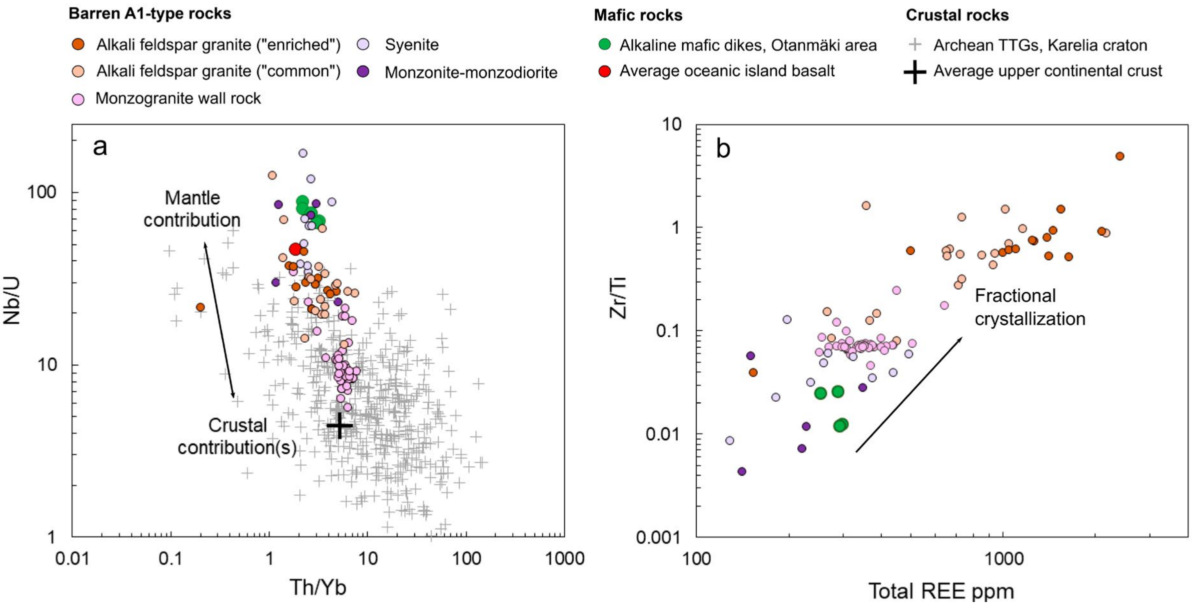

Figure 10. Trace element data for A1-type rocks and alkaline mafic dikes from the Otanmäki area. a) Nb/U vs Th/Yb diagram. b) Zr/Ti vs. total REE diagram. Compositions of average OIB (Sun & McDonough, 1989), a large number of samples representing TTGs in the Karelia craton (Rock geochemical database of Finland, Rasilainen et al., 2007) and average upper continental crust (Rudnick & Gao, 2003) are shown for comparison.

Ba-Sr-Eu-enriched or -depleted types (relative to REEs, barring Eu; Fig. 9c), which show either positive or negative Eu anomalies (Eu/Eu* = ~1.0–3.1 and ~0.4–0.9), respectively. The monzonite and monzodiorite exhibit patterns that are roughly similar to those of average OIB and alkaline mafic dikes from the Otanmäki area, expect that they are enriched in Ba, K, and Eu (Eu/Eu* = ~1.3–2.4) relative to REEs (expect Eu; Fig. 9d).

6.2. Mineralized rock units

The mineralized rocks both at Kontioaho and Katajakangas exhibit SiO_2 contents that are typical of granitic rocks (~66–71 wt.% and ~68–82 wt.%, respectively; Fig. 8a), although some samples with high calcite and/or fluorite contents show lower SiO_2. Based on their alkalinity, the mineralized samples can be classified as metaluminous (Fig. 8b). A geochemical affinity of the mineralized rocks to the AF granite is obvious from primitive mantle-normalized spidergrams, in which all mineralized rocks display pronounced depletions in Ba, Sr, Eu, P, Ti relative to REEs (except Eu), Nb-Ta, Th-U, and Zr-Hf (Figs. 9b, e, f). Also, compared to the AF granite, the mineralized rocks at Kontioaho and Katajakangas show similarly high Fe/Mg (FeO_{tot}/(FeO_{tot} + MgO) = ~0.8–1.0) and enrichment in LREE relative to HREE (LREE/HREE = ~3–6) and similarly negative Eu anomalies with Eu/Eu* of ~0.3–0.4 (Table 4; Fig. 11). However, they differ from the AF granite in having higher REE-HFSE and CaO and lower Al_2O_3 and total alkalies. In this respect, the Katajakangas dikes show the most extreme compositions, except for Zr, which displays the highest concentration in the mineralized rocks at Kontioaho (Table 4; Figs. 8a and 12a–c). There are also some important differences in FeO_{tot} as the mineralized rocks at Kontioaho and the enriched AF granite show higher FeO_{tot} contents compared to the Katajakangas mineralized dikes and common AF granite (Fig. 12d). Fluorine correlates well with REE-HFSE and CaO in the Kontioaho mineralized body, but in contrast, the Katajakangas mineralized dikes have low contents of F (Fig. 13a). Instead, CO_2 and S are high in some

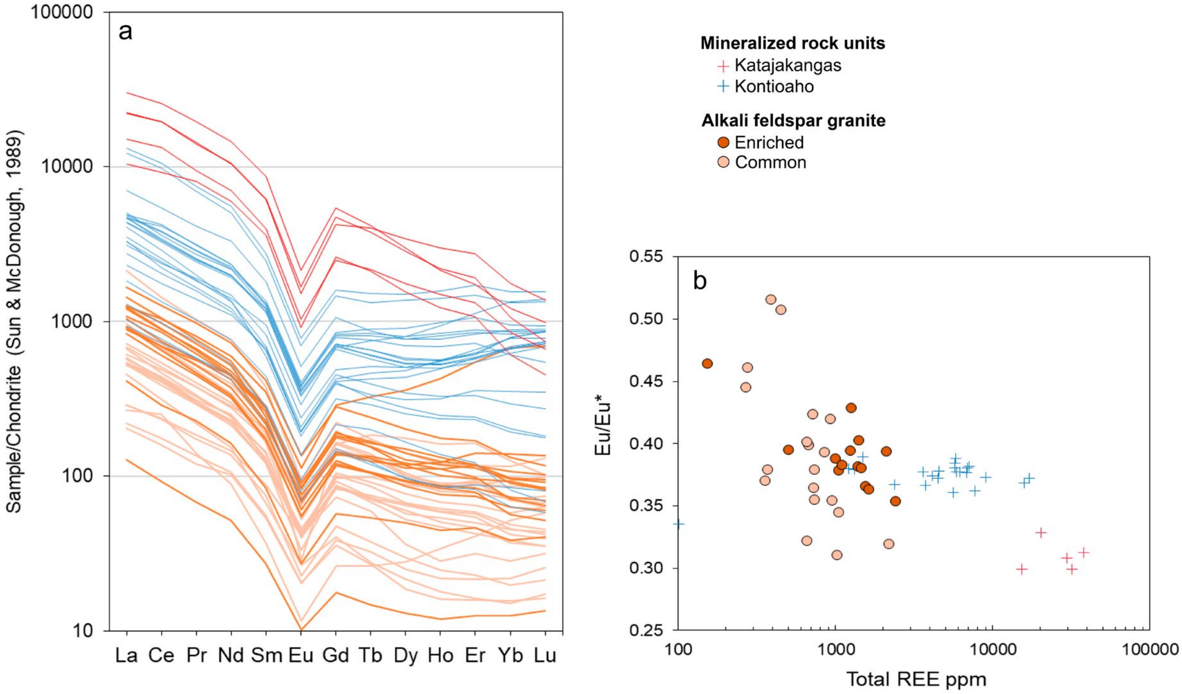

Figure 11. Mineralized samples from Kontioaho and Katajakangas and associated alkali feldspar granite plotted on a) chondrite-normalized REE variation diagram and b) Eu/Eu* vs. total REE diagram. Eu anomalies (Eu/Eu*) in a) have been calculated as Eu_{CN}/Eu* where Eu* is $\sqrt{(Sm_{CN} \times Gd_{CN})}$. Normalizing values are from Sun and McDonough (1989).

mineralized dikes at Katajakangas, and together with elevated F, CO_2 and S are also high in the barren wall rock containing metasomatite-bands and calcite±fluorite veins, although the available F data are limited (Fig. 13).

7. Isotopic studies

7.1. Zircon geochronology

In-situ SIMS dating was conducted on zircon grains separated from a sample from the Kontioaho occurrence (for the zircon separation procedure, see Electronic Appendix D). The mineral separation resulted in abundant subhedral-anhedral, stubby zircon grains with a length range of approximately 30–120 µm. In total, 35 spots from 29 zircons grains were analyzed. The analytical results of the probed zircon grains are listed and their BSE images illustrated in Electronic Appendix D, and a summary of the age data is presented in Table 5.

The porous domains in Kontioaho zircon grains have high U (320–1770 ppm) and Th (30–750 ppm) contents and contain texturally different domains, which yield different U-Pb isotope compositions. We identified three different domains (P1, P2, P3) by integrating the textural and chemical information with the gathered U-Pb isotope data (Table 5). The most obvious isotopic difference between the domain types concerns the $^{207}Pb/^{206}Pb$ dates, as illustrated in Fig. 14a. There is a trend towards increasingly younger dates (from ca. 2.06 to 1.87 Ga) with an increasing amount of textural evidence for re-equilibration, such as porosity, number of cracks, Th-U-rich inclusions, or dark (REE-depleted) patches in BSE images.

The first group (P1) yields the oldest $^{207}Pb/^{206}Pb$ dates of ca. 2.06–2.03 Ga obtained from relatively featureless, bright (REE- and U-rich) BSE domains. By rejecting three spots with high common lead, the remaining compositions (n = 5) are all reversely

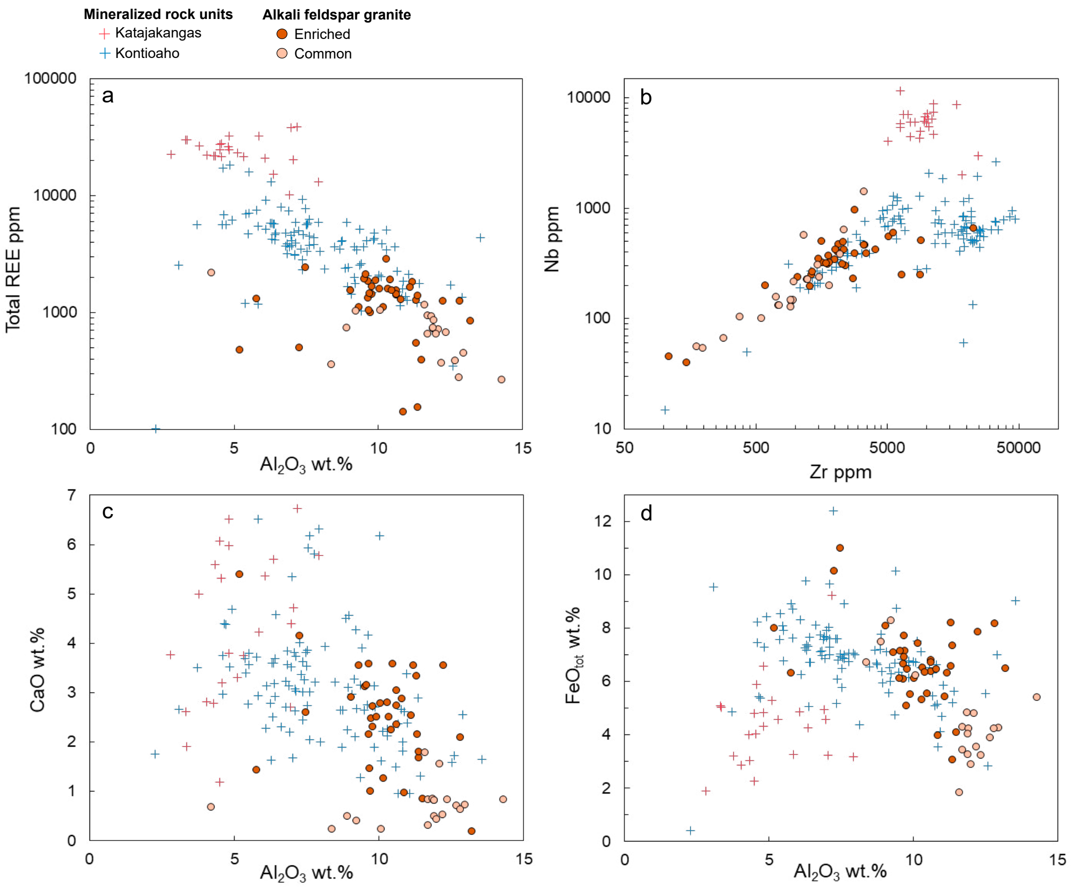

Figure 12. Major and trace element data for mineralized samples from Kontioaho and Katajakangas and associated alkali feldspar granite. a) Total REE vs. Al_2O_3 diagram. b) Nb vs. Zr diagram. c) CaO vs. Al_2O_3 diagram. d) FeO_{tot} vs. Al_2O_3 diagram.

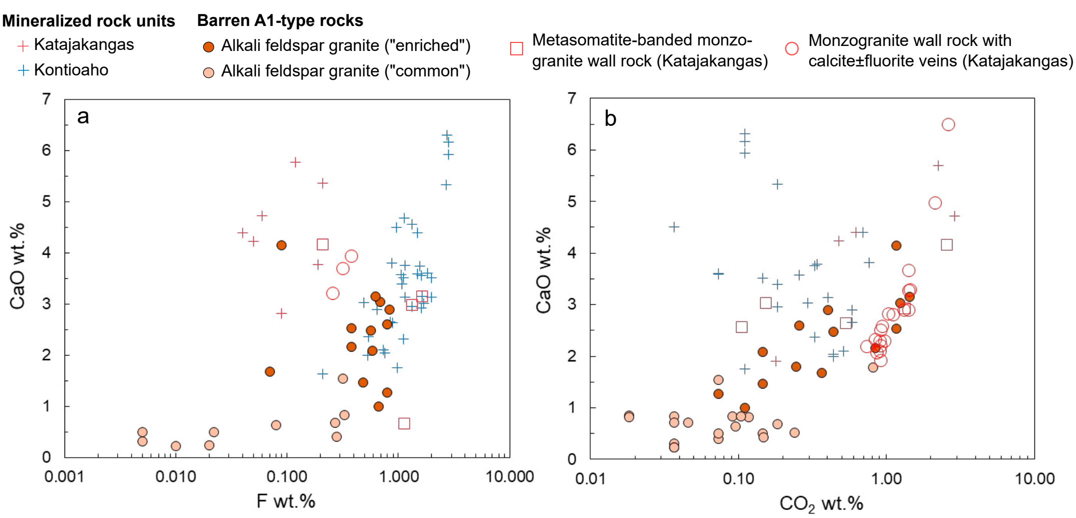

Figure 13. a) CaO vs. F and b) CaO vs. CO_2 diagrams for samples from the Kontioaho and Katajakangas Nb-Zr-REE mineralization, monzogranite wall rocks of the Katajakangas mineralized dikes with metasomatite bands and calcite±fluorite veins, and common and enriched-type alkali feldspar granite.

Table 5. Results of U-Pb SIMS dating of zircon grains from the Kontioaho mineralization.

Zircon domain type	Chemical and textural features of the analyzed domains	Range in $^{207}Pb/^{206}Pb$ ages	*$^{207}Pb/^{206}Pb$ age(s)	Remarks
P1	Clear, bright (REE- and U-rich) domains in BSE images showing the least amount of re-equilibration textures (e.g. porosity, Th-U-rich micro-inclusions).	2037 – 2033 Ma	2036 ± 4 Ma	Age approaches the initial crystallization age of the zircon and mineralization event, possibly with only minor resetting of the precursor zircon U-Pb isotope system.
P2	Abundant micrometer-sized pores, Th-U-rich micro-inclusions and/or dark patches (REE-poor) in BSE images.	2024 – 1955 Ma	–	Pb/Pb ages reflect partially reset, texturally re-equilibrated areas in precursor zircon.
P3	Several micrometer-sized pores and inclusions, cracks, and/or patches of varying brightness in BSE images.	1915 – 1868 Ma	1896 ± 26 Ma	Age of the zircon re-equilibration event. Completely reset domains in the precursor zircon.
Overgrowth rims	Clear, nonporous, fractured and mostly darker in BSE images than the parent (porous) zircon.	1915 – 1712 Ma	1895 ± 20 Ma and 1819 ± 36 Ma	Overgrowths formed during metamorphism.

*error in ages are at the 2s level

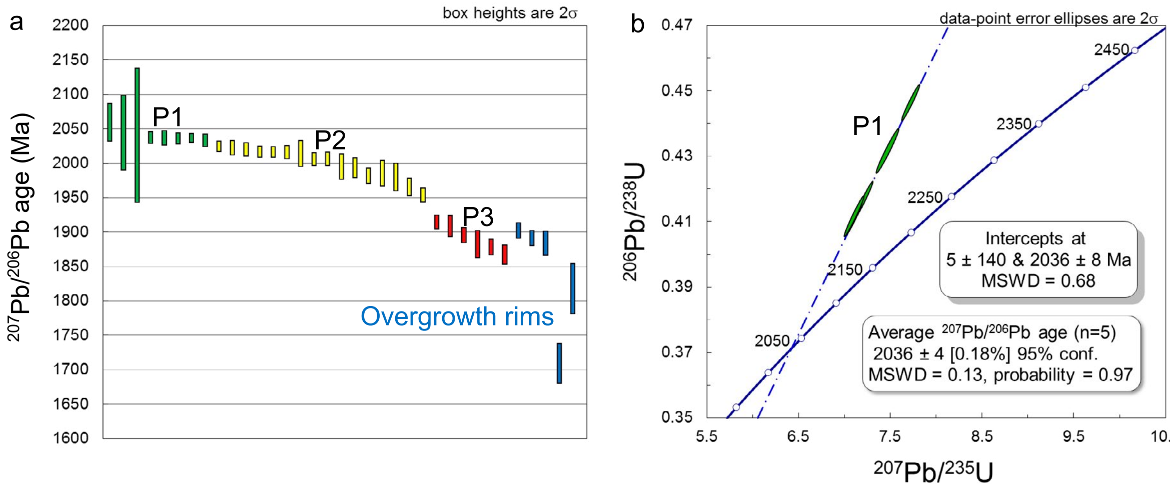

Figure 14. Results of SIMS U-Pb zircon dating from Kontioaho mineralization. a) $^{207}Pb/^{206}Pb$ dates for porous zircon domains and overgrowth rims (P1, P2, P3; for more details see Table 6 and for BSE images and data see Electronic Appendix D). b) Concordia diagram for analyses from porous P1 domains.

discordant, yielding an average $^{207}Pb/^{206}Pb$ age of 2036 ± 4 Ma (Table 5; Fig. 14b). The reverse discordance of the analyses casts some uncertainty on the validity of this age. However, it is highly likely that the reverse discordance is due to calibration bias caused by the significant compositional difference between the calibration zircon (91500) and the Kontioaho zircon. Even so, the credibility of the obtained ca. 2.04 Ga Pb/Pb age is corroborated by the plotting of the analyses along a regression line (Fig. 14b) that goes through the origin, and by the closeness of the age to the crystallization age of the AF granite in the Otanmäki area (ca. 2.04–2.05 Ga; Kärenlampi et al., 2019).

The second group (P2) of analyses (n = 16) is from zircon domains with abundant micron-sized pores, variable brightness in BSE images or cracks, and in some cases, remnants of oscillatory zoning. The U-Pb data for these points are all reversely discordant and define no obvious chord in the concordia diagram, with the scattered $^{207}Pb/^{206}Pb$ dates varying from ca. 2.02 to 1.95 Ga (Fig 14a.). These younger dates indicate that the zircon domains of the second group represent areas of isotopically more extensively reset zircon, which still carry some variably preserved memory of the pristine U-Pb isotope composition. It is noteworthy that similar zircon dates of ca. 1.96 to 2.03 Ga have previously been obtained for altered domains in zircon grains from the Otanmäki suite granites (Kärenlampi et al., 2019).

The third group (P3) of analyses (n = 6) represents textural domains in zircon grains that display the most altered appearance (Table 5) characterized by plentiful micron-sized pores, cracks, areas of variable brightness in BSE images, low total REE contents, and the lowest Th/U ratios detected in the porous zircon grains. The $^{207}Pb/^{206}Pb$ dates for the analyzed six points are significantly younger than those obtained from the P1 and P2 type domains, ranging from ca. 1.92 to 1.87 Ga (Fig. 14a). Three of the compositions are concordant (within error), yielding an average $^{207}Pb/^{206}Pb$ age of ca. 1896 ± 26 Ma, which coincides with the initiation of the Svecofennian orogeny and regional metamorphism (Lahtinen et al., 2015).

In addition to the dominant porous zircon domains, nonporous overgrowth rims were analyzed from five zircon grains. On the basis of SIMS analysis, these overgrowths have 53–834 ppm U, 0–94 ppm Th, and Th/U ratios that are comparable to those of the P2 and P3 type domains. Three of the compositions are concordant (within error) at ca. 1.90–1.89 Ga, giving an average $^{207}Pb/^{206}Pb$ age of 1895 ± 20 Ma. In addition, one composition is concordant at ca. 1.82 Ga and one is highly discordant.

7.2. Sm-Nd isotopic compositions

Neodymium isotope compositions were measured for 14 whole-rock samples, which include samples from the two Nb-Zr-REE occurrences, surrounding barren A1-type rocks, and enclosed Paleoproterozoic metasedimentary rocks (Table 6; for sample locations and descriptions, see Electronic Appendix E). The analytical method that was used for individual samples is indicated in Table 6. For comparative purposes, we utilize Sm-Nd isotope data reported by Huhma et al. (2018) for 2.06 Ga gabbros from the study area and data retrieved from the Isotope Database of Finland (www.gtk.hakku.fi/en) for the late Archean TTGs in eastern Finland.

The samples from the mineralized rocks and barren Otanmäki suite igneous rocks (monzodiorite, monzonite, syenite, monzogranite, and AF granite) all have relatively high LREE contents and their initial $\boldsymbol{\varepsilon}_{Nd}$(2050 Ma) values range from +2.6 to -1.3 (Table 6). The intermediate rock samples show positive values (+2.6 to 1.3), which are only slightly lower than the estimated value for depleted mantle at 2050 Ma (+3.4) but much higher than ε_{Nd}(2050 Ma) of Archean TTGs in the surrounding bedrock (avg. -10; Fig. 15). This indicates that these rocks were derived essentially from a mantle source rather than from some older, highly fractionated material, such as TTGs in the Archean basement. The AF granite and monzogranite give ε_{Nd}(2050 Ma) values of +0.6 to -0.9 and -1.3, respectively, which are somewhat lower than those of the intermediate rocks. This suggests that the granites record a greater amount of material contribution from an older felsic crust, consistent with their trace element signature (Fig. 10a). The ε_{Nd}(2050 Ma) values (0.0 to -1.1; Fig. 15, Table 6) of the mineralized samples are comparable to those of the AF granite. The 2.06 Ga Fe-Ti-V ore-bearing gabbros at Otanmäki show ε_{Nd}(2060 Ma) values from -0.5 to -0.9, being in this respect similar to the barren A1-type granites and mineralized samples, whereas the Paleoproterozoic metapsammites yield significantly lower ε_{Nd}(2050 Ma) values of -3.4 to -3.5 (Fig. 15).

Table 6. Sm-Nd isotope data for samples from the Kontioaho and Katajakangas mineralization and associated rocks in the Otanmäki area.

Rock type	Sample	Analytical method	Nd (ppm)	Sm (ppm)	$^{143}Nd/^{144}Nd$	± 2σm	$^{147}Sm/^{144}Nd$	ε_{Nd}	t (Ma)	$\varepsilon_{Nd}(t)$	
Katajakangas mineralized dike	**KK1**	HR-MC-ICP-MS	6312	1251	0.511547	16	0.1198	-21.3	2050	-1.1	± 0.3
Katajakangas mineralized dike	**KK2**	ICP-SFMS	2955	565	0.511524	4	0.1156	-21.7	2050	-0.4	± 0.1
Kontioaho mineralization	**KO2**	ICP-SFMS	2137	361	0.511363	7	0.1021	-24.9	2050	0.0	± 0.1
(high-grade)	**#2**	ICP-SFMS	2138	362	0.511368	5	0.1024	-24.8	2050	0.0	± 0.1
Monzogranite wall rock	**MG1**	HR-MC-ICP-MS	50	8.7	0.511362	5	0.1067	-24.9	2050	-1.3	± 0.1
Alkali feldspar granite ("enriched")	**AG1**	ICP-SFMS	201	40	0.511548	6	0.1191	-21.3	2050	-0.9	± 0.1
Alkali feldspar granite ("common")	**1-OTA**	ID-TIMS	105	20	0.511475	11	0.1126	-22.7	2050	-0.6	± 0.2
Alkali feldspar granite ("common")	**A100**	ID-TIMS	100	20	0.511568	10	0.1205	-20.9	2050	-0.9	± 0.2
Alkali feldspar granite ("common")	**A1149**	ID-TIMS	37	6.6	0.511470	20	0.1076	-22.8	2050	0.6	± 0.4
	#2	ID-TIMS	37	6.6	0.511454	10	0.1071	-23.1	2050	0.4	± 0.2
Syenite	**S2**	HR-MC-ICP-MS	59	9.5	0.511418	14	0.0980	-23.8	2050	2.1	± 0.3
Syenite	**S1**	HR-MC-ICP-MS	38	7.0	0.511591	9	0.1095	-20.4	2050	2.5	± 0.2
Monzonite	**M2**	HR-MC-ICP-MS	33	6.9	0.511767	6	0.1268	-17.0	2050	1.3	± 0.1
Monzodiorite	**M1**	HR-MC-ICP-MS	46	8.3	0.511582	6	0.1085	-20.6	2050	2.6	± 0.1
Metapsammite	**Ka4**	ID-TIMS	6.4	1.3	0.511493	11	0.1244	-22.3	2050	-3.4	± 0.2
Metapsammite	**Ka5**	ID-TIMS	7.0	1.5	0.511495	20	0.1249	-22.3	2050	-3.5	± 0.4

The ε_{Nd} (present day) and $\varepsilon_{Nd}(t)$ values were calculated after DePaolo and Wasserburg (1976) using $\lambda^{147}Sm = 6.54 \cdot 10^{-12}\ a^{-1}$, $^{147}Sm/^{144}Nd = 0.1966$ and $^{143}Nd/^{144}Nd = 0.512640$ for the present CHUR. # = duplicated analysis. HR-MC-ICP-MS = high resolution multi collector inductively coupled mass spectrometry, ICP-SFMS = inductively coupled sector field mass spectrometry, ID-TIMS = isotope dilution thermal ionization mass spectrometry.

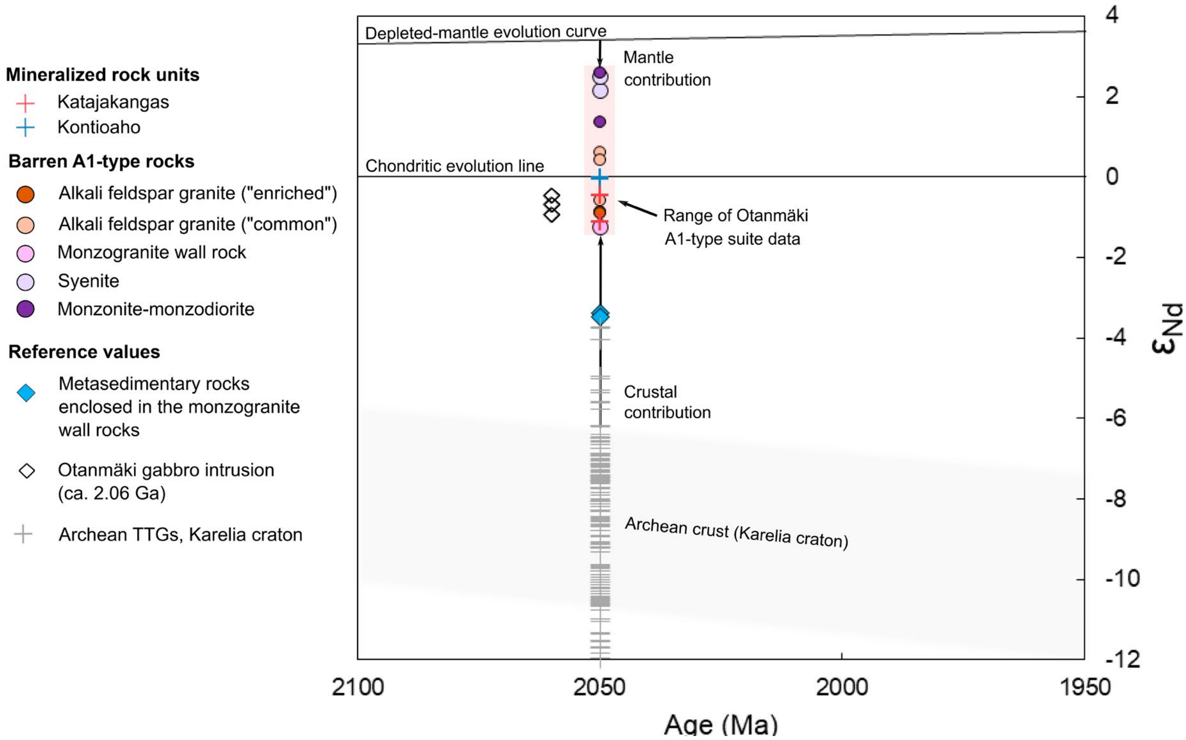

Figure 15. ε_{Nd} vs. age (Ma) diagram for samples from the Kontioaho and Katajakangas mineralized rock units and associated Otanmäki suite A1-type rocks. For comparison, also shown are data for samples from the metasedimentary unit enclosed in the monzogranite body, ca. 2.06 Ga Otanmäki gabbro intrusion (Huhma et al., 2018), and Archean TTGs from the Karelia craton (Isotope database of Finland, www.gtk.hakku.fi/en). Depleted mantle evolution curve after DePaolo (1981).

8. Discussion

8.1. Nb-Zr-REE mineral assemblage

In the Otanmäki Nb-Zr-REE occurrences, the REEs are dominantly incorporated into allanite-(Ce), Zr into zircon, and Nb into titanite and/or various Nb-REE-Th-U oxide minerals. These mineral assemblages are clearly simpler than in many other granite-related Nb-Zr-REE occurrences, which often contain a plethora of minerals including Nb-Zr-REE-bearing fluorocarbonates (bastnäsite, parisite, synchysite), phosphates (monazite, xenotime), silicates (gittinsite, elpidite, zircon, gadolinite, chevkinite, allanite, iimoriite, cerite, kainosite, eudialyte), oxides (e.g., fergusonite, pyrochlore, columbite), and halides (e.g., fluorite, gagarinite, tveitite). These complex mineral assemblages occur in rocks that typically display variable replacement textures/pseudomorphs as a result of subsolidus hydrothermal alteration (e.g., Kynicky et al., 2011; Kempe et al., 2015; Gladkochub et al. 2017; Siegel et al., 2018; Morgenstern et al., 2018). In contrast, in the Otanmäki mineralization, the Nb-Zr-REE-bearing minerals only display textures and compositions of pervasive metamorphic re-equilibration.

Our literature review reveals that allanite-zircon-titanite mineral assemblages are common in relatively low-alkalinity, oxidized and metaluminous or slightly peraluminous granitoids with high Ca contents but are rare in low-Ca peraluminous or peralkaline granitoids, which instead crystallize REE phosphates, REE-Ti silicates (e.g., chevkinite), ilmenite, and/or complex zirconosilicates (e.g., elpidite) (Cuney & Friedrich, 1987; Wones, 1989; Bea, 1996; Petrik et al., 1995; Broska et al., 2000; Spicer, 2001; Hoshino et al., 2006; Vlach & Gualda, 2007; McDonald et al., 2009, 2019; Kynicky et al., 2011; Watanabe et al., 2016). Based on experimental and empirical evidence (e.g., Cuney & Friedrich 1987; Spicer, 2001; Vlach & Gualda, 2007; Klimm et al., 2008; McDonald et al., 2009; Budzyń et al., 2011; Papoutsa & Pe-Piper, 2013; Li & Zhou, 2018), allanite should be the most stable REE phase in Ca-, Si-, Fe-, Al-rich and (metaluminous) alkali- and P-poor and relatively low-fCO_2 systems, such as the mineralization at Otanmäki. Our textural observations support this interpretation as allanite-(Ce) occurs mostly as fine-grained, discrete grains clustered together in bands or other agglomerations without evidence for reactions or a systematic association with potential precursor phases or their decomposition products. The allanite-forming and -consuming reactions described in previous studies involve monazite (e.g., Finger et al., 1998; Gieré & Sorensen, 2004; Li & Zhou, 2017; Andersson et al., 2018), REE-Ti silicates (the chevkinite-group minerals; McDonald et al., 2012; Bagiński & McDonald, 2013; McDonald et al., 2019), or REE fluorocarbonates (e.g., Savel'eva & Karmanov, 2008, Papoutsa & Pe-Piper, 2013; McDonald et al., 2015). A primary origin of the allanite-(Ce) in the Otanmäki mineralization is also supported by the fact that allanite has a wide P-T stability field under typical metamorphic fluid conditions (Liu et al., 1999; Hermann, 2002; Gieré & Sorensen, 2004; Chen & Zhou, 2014), indicating that it could have survived the amphibolite-facies regional metamorphism of the Otanmäki area. Thus, our observations coupled with findings of previous studies suggest that the mineral species/assemblages in the Otanmäki Nb-Zr-REE occurrences are essentially primary and persisted through metamorphic re-equilibration, though with some textural and compositional changes.

8.2. Processes of Nb-Zr-REE enrichment

The two Nb-Zr-REE mineralized zones in the Otanmäki area are located within a body of peraluminous monzogranite gneiss, which is surrounded by gneissic peralkaline to metaluminous AF granite and intermediate plutonic rocks, including syenite and monzonite-monzodiorite. The mineralized rocks occur as sharply bound dikes (Katajakangas) and a sheet-like intrusive body (Kontioaho), which demonstrates that the mineralization event postdates the emplacement of the surrounding peraluminous monzogranite phase. On the basis of its whole-rock chemistry and Sm-Nd isotope characteristics and zircon U-Pb age, the mineralization seems to be genetically unrelated to its monzogranite host rock but rather is linked to the close-by AF granite. The AF granite at Otanmäki is distinguished from the associated monzogranite and intermediate rocks by several geochemical features indicating of extensive crystal fractionation, such as high Zr/Ti and total REE contents, as well as strong depletions in Sr, Ba, Ti, P, and Eu relative to Zr, Nb, Rb and REEs (except Eu). Such geochemical characteristics are often observed in peralkaline igneous rocks thought to represent the most evolved melts produced via fractional crystallization of mafic parental magmas (cf. Eby et al., 1992; Zozulya et al., 2009; Shellnut et al., 2011; Dostal & Shellnut, 2016; Jeffery & Gertisser, 2018). The ε_{Nd}(2050 Ma) values of the Otanmäki AF granite, which range from +0.6 to -0.9, also support their generation via fractionation of a mantle-derived mafic magma, rather than by partial melting of older crustal rocks. However, as the ε_{Nd}(2050 Ma) values of the AF granite are lower than those of the associated intermediate rocks (+2.6 to +1.3), they still evince a small degree of crustal assimilation.

In general, generation of REE-HFSE mineralization associated with granitic rocks is attributed either to magmatic or hydrothermal processes or their combination (e.g., Kovalenko et al., 1995; Schmitt et al., 2002; Salvi & Williams-Jones, 2005; Kynicky et al., 2011; Sun et al., 2013; Kempe et al., 2015). Many observations argue against extensive hydrothermal activity in the genesis of the Otanmäki Nb-Zr-REE mineralization. For example, the sharp boundaries of the mineralized rock units and magmatic-like QAP mineralogy and unaltered whole-rock compositions of wall rock monzogranite samples, even at the immediate contacts to the mineralization, do not support processes that involved percolation of large amounts of fluid rich in aggressive ligands and rare metals (cf. Kempe et al., 2015). As noted above, the compositions of the AF granite and the mineralized rocks show a general pattern of REE-HFSE and SiO_2 enrichment associated with a decrease in Al_2O_3 and total alkali contents, which is most consistent with interpretation that the enrichment in Nb-Zr-REE was related to the magmatic evolution of the associated AF granite. A process involving extensive fractionation of alkali feldspar seems to be the only realistic magmatic mechanism to produce the observed geochemical trends, as all the above-mentioned depleted elements have high feldspar/melt partition coefficients and feldspar is the only mineral able to effectively remove Al_2O_3 from a granitic magma.

We tested the hypothesis of feldspar fractionation by simple mass-balance calculations (for details see Electronic Appendix F) in which we modeled crystallization of alkali feldspars ($NaAlSi_3O_8$ and $KAlSi_3O_8$, 50:50) in eight separate steps, with each of them involving 8% removal of alkali feldspar from the magma. As the starting magma composition, we used an average composition of common (peralkaline) AF granite calculated from whole-rock analyses. We focused on SiO_2, Al_2O_3, Na_2O, K_2O, FeO_{tot} and CaO. The calculations show that feldspar removal results in an Al_2O_3 depletion and SiO_2 enrichment similar to that observed in the mineralized rocks, but it cannot replicate their variations in Na_2O, K_2O, FeO_{tot} and CaO (Fig. 16). Furthermore, alkali feldspar removal also causes an effective increase in the peralkalinity of the residual melt because alkali feldspar removes more Al from the melt relative to Na and K, lowering the A/NK ratio (Fig. 16d). Thus, alkali feldspar separation cannot alone explain the bulk metaluminous compositions of the mineralized rocks. A peralkaline melt can evolve towards a metaluminous composition if the A/NK ratio of the melt is somehow increased and simultaneously its A/CNK ratio stays relatively constant. In a magmatic system from which alkali feldspars are removed the only way to increase A/NK is by increasing the Ca content of the melt and lowering the Na or K contents without causing additional loss of Al. In a peralkaline melt, an increase in A/NK can be achieved by crystallization of Na-rich clinopyroxene or amphibole (e.g., aegirine, riebeckite), which incorporate significant Na, Fe and Si but very little Al or Ca. Thus, the likely explanation for the discrepancy between the model curve and the data is related to separation of mafic minerals. Therefore, we improved the model by adding aegirine ($NaFeSi_2O_6$), quartz (SiO_2), and magnetite (Fe_2O_4) to the crystallizing phases, as they are common minor to major minerals in the AF granite at Otanmäki (Table 1). The subsequent several iterations showed that a two-stage fractionation model is required to construct a curve that fits with the data of the Kontioaho and Katajakangas mineralized rock units. The first stage involves 53% crystallization of a common AF granite parental magma, involving removal of alkali feldspar, quartz and aegirine (60:30:10, respectively). The second stage involves separation and subsequent near complete crystallization of the residual melt of the first stage, involving removal of alkali feldspar, quartz, aegirine, and magnetite (69:14:13:4, respectively). The resulting model curve (Fig. 16) explains the major element characteristics of the mineralized rocks, including their metaluminous bulk composition, but also the evolution from common to enriched AF granite. The model curve also reveals that the closest compositions to the Katajakangas dikes are achieved via 99% of crystallization whereas the Kontioaho compositions are already reached at ~73–86% of crystallization in the second crystallization stage (Fig. 16).

Results of our modeling are compatible with the observed volumes of the mineralized rocks, which are notably larger at Kontioaho compared to Katajakangas, being consistent with a fractional crystallization process in which more highly evolved melts occupy smaller volumes. In addition, the bulk of fractionated solids removed in the two-stage fractionation model consist of 66% alkali feldspar, 19% quartz, 12% aegirine, and 3% magnetite, which is in good agreement with the actual modal compositions of the AF granite (65–75% alkali feldspars, 15–30% quartz, and 5–15% mafic minerals). Although chemical data on the feldspars and mafic silicates are not available, we used compositions of Ca-free albite and aegirine in our calculations. This was done because our preliminary test iterations showed that even a minor amount of CaO (~1–5 wt.%) in these phases prevents replication of the CaO-enriched bulk compositions of the mineralized rocks (see Electronic Appendix F). However, it is unrealistic that pure albite and aegirine crystallized from a peralkaline granite magma as, in peralkaline granite, these minerals typically contain a minor amount of CaO (e.g., Marks et al., 2003; Vilalva et al., 2016). This suggests that the CaO build-up in the Otanmäki granitic system was promoted by some additional factor(s) than extensive crystallization of Ca-poor mineral assemblages.

We also performed modeling of selected trace elements Ce, Y, Zr, and Nb using the Rayleigh equation, with the mineral/melt partition coefficients (D) taken from the EarthRef database (https://earthref.org/KDD/). We calculated bulk partition coefficients (D_b) using the same phase proportions as in the above discussed two-stage fractionation model (for the full input and output data, see Electronic Appendix F). Figure 17 displays calculated variations in the Ce, Y, Zr and Nb abundances as a function of the degree of crystallization, together with model curves calculated assuming bulk D of zero (D_0). For Ce and Y, the D_b curves indicate only a slight enrichment, failing to reach the extreme concentrations observed in the Kontioaho and Katajakangas mineralized rock units at the degrees of crystallization constrained by the major element calculations (Fig. 17a). In contrast, the D_0 curves provide a better fit, indicating that the REE enrichment was also promoted by some other factors than extensive crystallization. For Zr and Nb, the results are ambivalent. The calculated D_b and D_0 curves result in too high Zr and Nb compared to the concentrations in the Katajakangas dikes, suggesting that there was higher than expected compatibility of these elements during crystal fractionation. In the Kontioaho case, the Zr and Nb concentrations calculated using the D_b values have

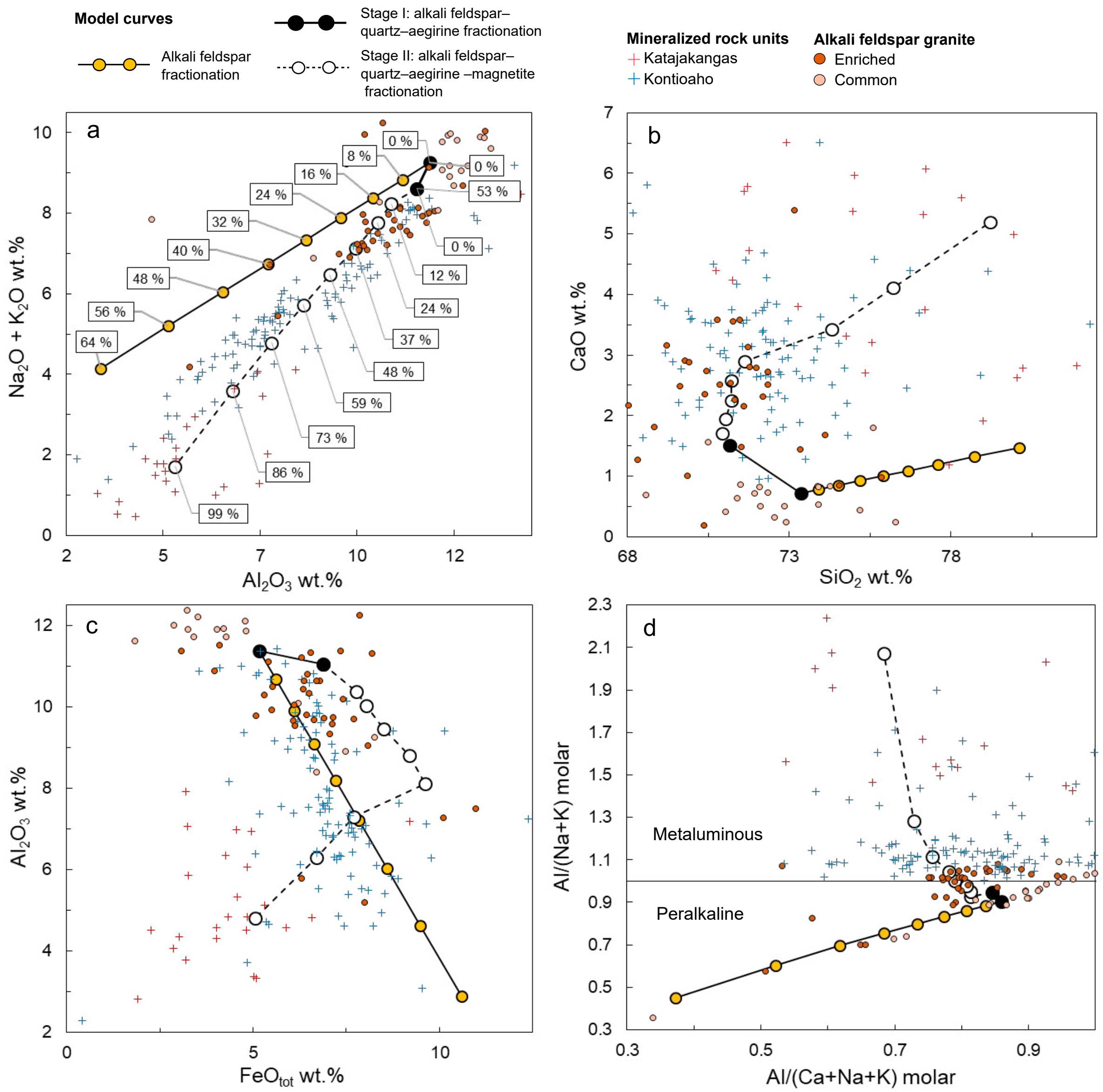

Figure 16. Variation diagrams presenting results of major and minor element modeling of fractional crystallization for Kontioaho and Katajakangas mineralized rocks. For comparison whole-rock data from both mineralized zones and Otanmäki common and enriched alkali feldspar granite are plotted. a) $Na_2O + K_2O$ vs. Al_2O_3 diagram. b) CaO vs. SiO_2 diagram. c) Al_2O_3 vs. FeO_{tot} diagram. d) Molar Al/(Na+K) vs. Al/(Ca+Na+K) diagram. The degree of crystallization in each crystallization step as in a). For modeling details and full input and output data, see Electronic Appendix F.

a relatively good fit with those of the Kontioaho low-grade rocks, but neither the D_b or D_0 curves intersect the values of the Kontioaho high-grade rocks, which have extremely high Zr relative to Nb (Fig. 17b).

Various volatiles (e.g., F, CO_2, S, H_2O) that are easily dissolved in evolved alkali-rich silicate melts (cf. Dostal & Chatterjee, 1995; Agangi et al. 2010; Vasyukova & Williams-Jones, 2014) may also be an contributing factor to the observed Nb-Zr-REE enrichment in the Otanmäki mineralization. Fluoride is likely the most important agent because high F contents in peralkaline melts cause distortion of the aluminosilicate structure (Giordano et al., 2004; Zimova & Webb, 2007), allowing highly

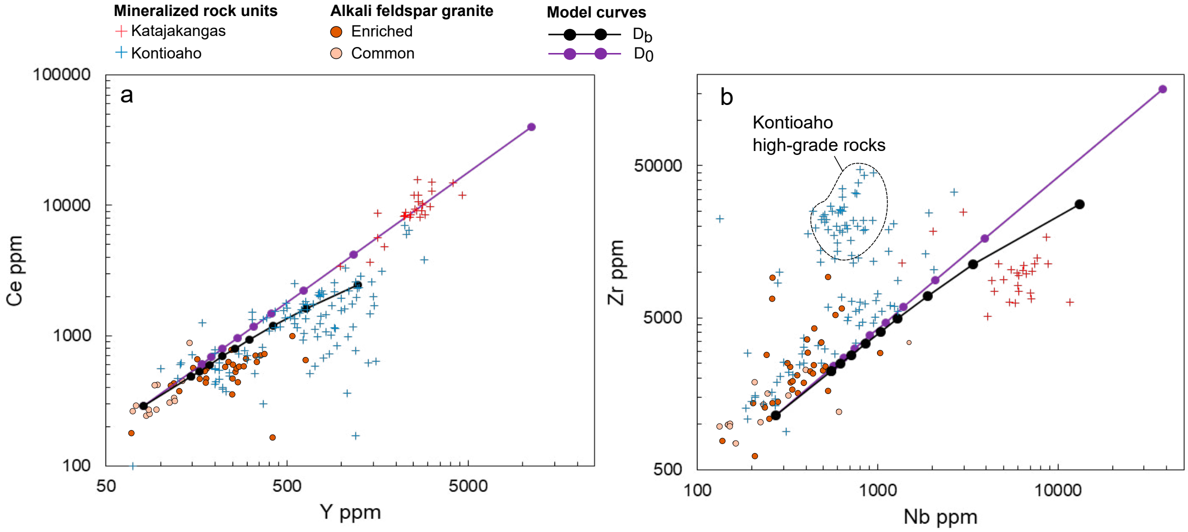

Figure 17. Variation diagrams presenting results of trace element modeling of fractional crystallization for the Kontioaho and Katajakangas mineralized rocks. For comparison whole-rock data from both mineralized zones and Otanmäki common and enriched alkali feldspar granite are plotted. a) Ce vs. Y diagram. b) Zr vs. Nb diagram. For the used partition coefficients, modeling details and full input and output data, see Electronic Appendix F.

charged cations (e.g., REE, HFSE) to form stable complexes with F and excess alkalies (Collins et al., 1982; Keppler, 1993; Stebbins & Zeng, 2000; Dolejš & Zajacz, 2018). Fluoride complexing may also be a factor in explaining the Ca build-up in the residual melts, as experiments suggest that Ca may form complexes with F (e.g., Luth, 1988; Stebbins & Zeng, 2000).

In the whole-rock data from the Otanmäki Nb-Zr-REE occurrences, F correlates well with REE and HFSE in the mineralized zones, indicating that REE and HFSE fractionated not only by crystal-melt equilibria but also by F complexation during crystal fractionation. However, there are some notable differences in the occurrence of F between the Kontioaho and Katajakangas mineralized zones, as the Kontioaho mineralized body is enriched in F (in fluorite), whereas the Katajakangas mineralized dikes have low contents of F (Fig. 13a) though F is present in the wall rocks at Katajakangas. This could indicate that the whole-rock compositions of the mineralized dikes do not fully record their emplacement stage F contents. The locally occurring F-, CO_2- and S-rich metasomatite bands and calcite±fluorite veins in the monzogranite wall rocks at Katajakangas suggest that some of the volatiles, which were initially transported by the dike-forming melts, were dispersed to the wall rocks, yet only after the decomposition of REE complexes and precipitation of REE-bearing minerals in the dikes, as judged from the unmineralized nature of the metasomatite-bands and calcite±fluorite veins. In addition, the small volumes of the metasomatite bands and calcite±fluorite veins indicate that the internally-derived magmatic fluid contribution to the mineralization was minor even during the late-stage evolution of the highly fractionated melts.

In the case of the Katajakangas mineralized dikes, it can also be argued that CO_2 and S, which typically occur in oxidized silicate melts as dissolved CO_3^{2-} and SO_4^{2-} ions (Carroll & Webster, 1994; Guillot & Sator, 2011; Ni & Keppler, 2013), also acted as important REE complexing ligands (cf. Shu & Liu, 2019; Zheng & Liu, 2019). There is evidence for an oxidized nature of the late-stage melts, including the calcic mineral assemblages of the mineralized rocks, as featured by allanite and titanite (see previous chapter) and the Eu/Eu* ratio, which exhibits only a slight decrease in the system, being comparable to the ratio in AF granite (-0.5 to 0.3; Fig. 11b). At Kontioaho, the process leading to the extreme Zr enrichment in the high-grade rocks is not entirely clear, but it is possible that a F-dominant composition of the volatile phase played a key role, noting the strong enrichment in F relative to CO_2 and S and Zr relative to Nb and REEs at Kontioaho compared to the Katajakangas dikes, which show an opposite relationship (Figs. 12 and 13). This interpretation is supported by some experiments demonstrating that in F-rich haplogranitic melts, the solubility of Zr is positively correlated with the F content of the melt, whereas in the case of Nb, such a relationship is almost absent (Aseri et al., 2015). This also implies that, in addition to crystal fractionation, the enrichment of REEs in the late-stage melts in the Otanmäki mineralization was promoted more by carbonate and sulfate complexation than fluoride complexation. The high-grade units of the Kontioaho mineralized body could also reflect an internal differentiation process, such as cooling and solidification inwards from the margins of the sheet-like intrusion, leading to inward concentration of the residual melt enriched in incompatible elements, most notably Zr. Such a process could also explain why the low-grade margins display modal compositions that are very similar to the thermal minimum in the quartz-albite-potassium feldspar system (35% quartz, 40% albite, 25% potassium feldspar; Johannes & Holtz, 1996), whereas the high-grade zones are strongly depleted in albite relative to potassium feldspar and quartz (Table 2).

A better understanding of the genesis of the Otanmäki mineralization could be attained by studying the major and trace element concentrations of feldspars and mafic silicates in the AF granite. The compositions of these minerals could serve as monitors of the magmatic evolution and magmatic REE enrichment, although the primary mineral chemistry of the AF granite at Otanmäki may have been disturbed during amphibolite-facies regional metamorphism. Another problem in understanding the Otanmäki mineralization is the limited data available from the actual root area of the mineralized dikes and the sheet-like intrusion, adding to the challenge of evaluating where and how the highly fractionated parental melts accumulated, what processes were involved in their escape from the extensively crystallized intrusions of peralkaline granite, and what was the temporal and spatial extent of these processes.

9. Conclusions

1) The Otanmäki area in central Finland hosts Nb-Zr-REE-enriched rocks within an igneous complex composed of ca. 2.04–2.06 Ga (A1-type) granites (monzogranite, alkali feldspar granite) and intermediate plutonic rocks (syenite, monzonite-monzodiorite). They exhibit trace element characteristics and whole-rock ε_{Nd}(2050 Ma) values from +2.6 to -1.3 that are consistent with derivation by differentiation of mantle-derived mafic magmas with variable interaction with crustal rocks.
2) The Nb-Zr-REE mineralization occurs as sharply bound, 0.1- to 1.4-m-thick dikes (Katajakangas) and a 30- to 50-m-thick, sheet-like intrusive body (Kontioaho) hosted by ca. 2.06 Ga peraluminous monzogranite gneiss. The rare metals of the mineralization are incorporated into allanite-(Ce), zircon, titanite, and Nb-REE-Th-U oxides, which likely represent the primary magmatic assemblage, though affected by extensive re-equilibration during the Svecofennian metamorphism at ca. 1.9–1.8 Ga.
3) The trace element characteristics, ε_{Nd}(2050 Ma) values (0.0 to -1.1), zircon U-Pb age (ca. 2.04 Ga) and numerical modeling support the interpretation that the mineralized rocks are genetically unrelated to their monzogranitic wall rock but were sourced from the nearby peralkaline to metaluminous alkali feldspar granite, which is dated at ca. 2.04–2.05 Ga.
4) The formation of the REE-HFSE enrichment is explained by a magmatic process involving an extreme degree of crystal fractionation of peralkaline granitic magmas. This process

produced metaluminous, high-silica residual melts enriched in REE-HFSE, Ca, and Fe relative to Na, K, and Al, with further REE-HFSE and Ca enrichment having been produced by the formation of fluoride, carbonate and sulfate complexes. These melts were parental to the Katajakangas dikes and the Kontioaho sheet-like intrusion emplaced into the peraluminous monzogranite capping the intrusions of peralkaline granite.

Acknowledgements

Financial support for this study was provided by the Advanced Materials Doctoral Programme (ADMA-DP) of the University of Oulu, the K.H. Renlund Foundation, and the Tauno Tönning Foundation. The field work was profoundly supported by Otanmäki Mine Oy (www.otanmaki.fi) and the CEO of the company, Jouko Jylänki, which is gratefully acknowledged. The NordSIMS facility is funded by the Swedish Research Council (infrastructure grant # 2017-00671), the Swedish Museum of Natural History and the University of Iceland; this is NordSIMS publication 647. Martin Whitehouse is thanked for U-Pb data reduction and Lev Ilinsky and Kerstin Lindén for laboratory assistance at NORDSIM. Andreas Bartzsch and Roland Würkert from the HIF and Sari Forss from the University of Oulu are thanked for the preparation of the samples used in MLA and EPMA. Leena Järvinen from the GTK is acknowledged for laboratory assistance. An anonymous reviewer, Tapio Halkoaho and the handling editor Ferenc Molnàr are thanked for their constructive comments that helped to improve this manuscript.

Supplementary data

Electronic Appendices A-F for this article are available via Bulletin of the Geological Society of Finland web page.

References

Agangi, A., Kamenetsky, V.S. & McPhie, J., 2010. The role of fluorine in the concentration and transport of lithophile trace elements in felsic magmas: Insights from the Gawler Range volcanics, South Australia. Chemical Geology 273, 314–325. https://doi.org/10.1016/j.chemgeo.2010.03.008

Äikäs, O., 1990. Thorium and niobium-lanthanide ore prospects in Otanmäki, Vuolijoki municipality. Geological Survey of Finland, Report M19/3431/-90/1/6, 34 p. (in Finnish)

Al-Ani, T., Molnar, F., Lintinen, P. & Leinonen, S., 2018. Geology and mineralogy of rare earth elements deposits and occurrences in Finland. Minerals 8(8). https://doi.org/10.3390/min8080356

Aleinikoff, J.N., Wintsch, R.P., Fanning, C.M. & Dorais, M.J., 2002. U-Pb geochronology of zircon and polygenetic titanite from the Glastonbury Complex, Connecticut, USA: an integrated SEM, EMPA, TIMS, and SHRIMP study. Chemical Geology 188, 125–147. https://doi.org/10.1016/S0009-2541(02)00076-1

Andersson, S.S., Wagner, T., Jonsson, E., Fusswinkel, T., Leijd, M. & Berg, J.T., 2018. Origin of the high-temperature Olserum-Djupedal REE-phosphate mineralisation, SE Sweden: A unique contact metamorphic-hydrothermal system. Ore Geology Reviews 101, 740–764. https://doi.org/10.1016/j.oregeorev.2018.08.018

Aseri, A.A., Linnen, R.L., Che, X.-C., Thibault, Y. & Holtz, F., 2015. Effects of fluorine on the solubilities of Nb, Ta, Zr and Hf minerals in highly fluxed water-saturated haplogranitic melts. Ore Geology Reviews 64, 736–746. https://doi.org/10.1016/j.oregeorev.2014.02.014

Atencio, D., Andrade, M.B., Christy, A.G., Gieré, R. & Kartashov, P.M., 2010. The pyrochlore supergroup of minerals: nomenclature. Canadian Mineralogist 48, 673–698. https://doi.org/10.3749/canmin.48.3.673

Bagiński B. & McDonald R., 2013. The chevkinite group: underestimated accessory phase from a wide range of parageneses. Mineralogia 44, 99–114. https://doi.org/10.2478/mipo-2013-0006

Bea, F., 1996. Residence of REE, Y, Th and U in granites and crustal protoliths; implication for the chemistry of crustal melts. Journal of Petrology 37, 521–552. https://doi.org/10.1093/petrology/37.3.521

Bedrock of Finland – DigiKP. Digital map database (Electronic resource). Espoo: Geological Survey of Finland (13 September 2019), Version 2.2., available at: https://gtkdata.gtk.fi/Kalliopera/index.html

Bernau, R. & Franz, G., 1987. Crystal chemistry and genesis of Nb-, V-, and Al-rich metamorphic titanite from Egypt and Greece. Canadian Mineralogist 25, 695–705.

Broska, I., Petrik, I. & Williams, C.T., 2000. Coexisting monazite and allanite in peraluminous granitoids of the Tribec Mountains, Western Carpathians. American Mineralogist 85, 22–32. https://doi.org/10.2138/am-2000-0104

Budzyń, B., Harlov, D.E., Williams, M.L. & Jercinovic M.J., 2011. Experimental determination of stability relations between monazite, fluorapatite, allanite, and REE-epidote as a function of pressure, temperature, and fluid composition. American Mineralogist 96, 1547–1567. https://doi.org/10.2138/am.2011.3741

Carroll, M.R. & Webster, J.D., 1994. Solubilities of sulfur, noble gases, nitrogen, chlorine, and fluorine in magmas. In: Carroll, M.R., Holloway, J.R. (eds.), Reviews in Mineralogy, Volume 30. Washington DC, Mineralogical Society of America, pp. 231–279.

Carswell, D.A., Wilson, R.N. & Zhai, M., 1996. Ultra-high pressure aluminous titanite in carbonate-bearing eclogites at Ahuanghe in Dabieshan, central China. Mineralogical Magazine 60, 461–471. https://doi.org/10.1180/minmag.1996.060.400.07

Černý, P. & Ercit, T.S., 1989. Mineralogy of niobium and tantalum: crystal chemical relationships, paragenetic aspects and their economic implications. In: Möller, P., Černý, P., Saupé, F. (eds.), Lanthanides, Tantalum and Niobium. Springer-Verlag, Berlin, Heidelberg, pp. 28–79.

Charalampides, G., Vatalis, K.I., Apostoplos, B. & Ploutarch-Nikolas, B., 2015. Rare earth elements: industrial applications and economic dependency of Europe. Procedia Economics and Finance 24, 126–135. https://doi.org/10.1016/S2212-5671(15)00630-9

Chen, W.T. & Zhou, M.F., 2014. Ages and compositions of primary and secondary allanite from the Lala Fe-Cu deposit, SW China: implications for multiple episodes of hydrothermal events. Contributions to Mineralogy and Petrology 168, 1043. https://doi.org/10.1007/s00410-014-1043-1

Collins, W.J., Beams, S.D., White, A.J.R. & Chappell, B.W., 1982. Nature and origin of A-type granites with particular reference to Southeastern Australia. Contributions to Mineralogy and Petrology 80, 189–200. https://doi.org/10.1007/BF00374895

Cuney, M. & Friedrich, M., 1987. Physicochemical and crystal-chemical controls on accessory mineral paragenesis in granitoids: implications for uranium metallogenesis. Bulletin Minéralogie 110, 235–247. https://doi.org/10.3406/bulmi.1987.7983

DePaolo, D.J., 1981. Neodymium isotopes in the Colorado Front Range and crust-mantle evolution in the Proterozoic. Nature 291, 193–196. https://doi.org/10.1038/291193a0

DePaolo, D.J. & Wasserburg, G.J., 1976. Nd isotopic variations and petrogenetic models. Geophysical Research Letters 3, 249–252. https://doi.org/10.1029/GL003i005p00249

Dollase, W.A., 1971. Refinement of the crystal structures of epidote, allanite and hancockite. American Mineralogist 56, 447–464.

Dostal, J. & Chatterjee, A.K., 1995. Origin of topaz-bearing and related peraluminous granites of the Late Devonian Davis Lake pluton, Nova Scotia, Canada: crystal versus fluid fractionation. Chemical Geology 123, 67–88. https://doi.org/10.1016/0009-2541(95)00047-P

Dostal, J. & Shellnut, G.J., 2016. Origin of peralkaline granites of the Jurassic Bokan Mountain complex (southeastern Alaska) hosting rare metal mineralization. International Geological Review 58, 1–13. https://doi.org/10.1080/00206814.2015.1052995

Dolejš, D. & Zajacz, Z., 2018. Halogens in silicic magmas and their hydrothermal systems. In: Harlov, D., Aranovich, L. (eds.), The Role of Halogens in Terrestrial and Extraterrestrial Geochemical Processes. Springer Geochemistry, Springer, Cham, pp. 431–543. https://doi.org/10.1007/978-3-319-61667-4_7

Eby, G.N., Krueger, H.W. & Creasy, J.W., 1992. Geology, geochronology, and geochemistry of the White Mountain batholith, New Hampshire. In: Puffer, J.H., Ragland, P.C. (eds.), Eastern North American Mesozoic Magmatism. Geological Society of America, Special Paper 268, 379–397. https://doi.org/10.1130/SPE268-p379

Ercit, T.S., 2005. Identification and alteration trends of granitic-pegmatite hosted (Y,REE,U,Th)–(Nb,Ta,Ti) oxide minerals: a statistical approach. Canadian Mineralogist 43, 1291–1303. https://doi.org/10.2113/gscanmin.43.4.1291

Finger, F., Broska, I., Roberts, M.P. & Schermaier, A., 1998. Replacement of primary monazite by apatite-allanite-epidote coronas in an amphibolite facies granite gneiss from the eastern Alps. American Mineralogist 83, 248–258. https://doi.org/10.2138/am-1998-3-408

Gieré, R. & Sorensen, S.S., 2004. Allanite and other REE-rich epidote-group minerals. Reviews in Mineralogy and Geochemistry 5, 431–493. https://doi.org/10.2138/gsrmg.56.1.431

Giordano, D., Romano, C., Dingwell, D.B., Poe, B. & Behrens, H., 2004. The combined effects of water and fluorine on the viscosity of silicic magmas. Geochimica et Cosmochimica Acta 68, 5159-5168. https://doi.org/10.1016/j.gca.2004.08.012

Gladkochub, D.P., Donskaya, T.V., Sklyarov, E.V., Kotov, A.B., Vladykin, N.V., Pisarevsky, S.A., Larin, M.A., Salnikova, E.B., Saveleva, V.B., Sharygin, V.V., Starikova, A.E., Tolmacheva, E.V., Velikoslavinsky, S.D., Mazukabzov, A.M., Bazarova, E.P., Kovach, V.P., Zagornaya, N.Y., Alymova, N.V. & Khromova, E.A., 2017. The unique Katugin rare-metal deposit (southern Siberia): constraints on age and genesis. Ore Geology Reviews 91, 246–263. https://doi.org/10.1016/j.oregeorev.2017.10.002

Goodenough, K.M., Wall, F. & Merriman, D., 2017. The rare earth elements: demand, global resources, and challenges for resourcing future generations. Natural Resources Research 27, 201–216.
https://doi.org/10.1007/s11053-017-9336-5

Guillot, B. & Sator, N., 2011. Carbon dioxide in silicate melts: A molecular dynamics simulation study. Geochimica et Cosmochimica Acta 75, 1829–1857.
https://doi.org/10.1016/j.gca.2011.01.004

Hermann, J., 2002. Allanite: thorium and light rare earth element carrier in subducted crust. Chemical Geology 192, 289–306.
https://doi.org/10.1016/S0009-2541(02)00222-X

Hoshino, M., Kimata, M., Shimizu, M., Nishida, N. & Fujiwara, T., 2006. Allanite-(Ce) in granitic rocks from Japan: genetic implications of patterns of REE and Mn enrichment. Canadian Mineralogist 44, 46–62.
https://doi.org/10.2113/gscanmin.44.1.45

Hoskin, P.W.O. & Schaltegger, U., 2003. The composition of zircon and igneous and metamorphic petrogenesis. Reviews in Mineralogy and Geochemistry 53, 27–62. https://doi.org/10.2113/0530027

Hugg, R., 1985a. Katajakangas. Geological mineral resource estimate. Rautaruukki Oy Exploration, Report OU 12/85, 13 p. (in Finnish)

Hugg, R., 1985b. Kontioaho. Geological mineral resource estimate. Rautaruukki Oy Exploration, Report OU 11/85, 14 p. (in Finnish)

Hugg, R. & Heiskanen, V., 1986. Exploration of Nb and lanthanides in the Otanmäki area. Rautaruukki Oy Exploration, Report OU 28/85, 6 p. (in Finnish)

Huhma, H., Hanski, E., Kontinen, A., Vuollo, J., Mänttäri, I. & Lahaye, Y., 2018. Sm–Nd and U–Pb isotope geochemistry of the Paleoproterozoic mafic magmatism in eastern and northern Finland. Geological Survey of Finland, Bulletin 405, 150 p.

Jeffery, J. & Gertisser, R., 2018. Peralkaline felsic magmatism of the Atlantic islands. Frontiers in Earth Science 6, 145. https://doi.org/10.3389/feart.2018.00145

Jeon, H. & Whitehouse, M.J., 2015. A critical evaluation of U–Pb calibration schemes used in SIMS zircon geochronology. Geostandards and Geoanalytical Research 39, 443–452.
https://doi.org/10.1111/j.1751-908X.2014.00325.x

Johannes, W. & Holtz, F., 1996. Petrogenesis and experimental petrology of granitic rocks. In: Wyllie, P.J, El Goresy A., von Engelhardt, W., Hahn, T. (eds.), Minerals and Rocks. Springer- Verlag, Berlin, 335 p.

Kärenlampi, K., Kontinen, A., Huhma, H. & Hanski, E., 2019. Geology, geochronology and geochemistry of the 2.05 Ga gneissic A1-type granites and related intermediate rocks in central Finland: implication for the tectonic evolution of the Karelia craton margin. Bulletin of the Geological Society of Finland 91, 35–73.
https://doi.org/10.17741/bgsf/91.1.002

Kempe, U., Möckel, R., Graupner, T., Kynicky, J. & Dombon, E., 2015. The genesis of Zr-Nb-REE mineralization at Khalzan Buregte (Western Mongolia) reconsidered. Ore Geology Reviews 64, 602–625.
http://dx.doi.org/10.1016/j.oregeorev.2014.05.003

Keppler, H., 1993. Influence of fluorine on the enrichment of high field strength trace elements in granitic rocks. Contributions to Mineralogy and Petrology 114, 479–488.

Klimm, K., Blundy, J. & Green, T.H., 2008. Trace element partitioning and accessory phase saturation during H_2O-saturated melting of basalt with implications for subduction zone chemical fluxes. Journal of Petrology 49, 523–553.
https://doi.org/10.1093/petrology/egn001

Kovalenko, V.I., Tsaryeva, G., Goreglyad, A.V., Yarmolyuk, V.V., Troitsky, V.A., Hervig, R.L. & Farmer, G.L., 1995. The peralkaline granite-related Khaldzan-Buregtey rare metal (Zr, Nb, Ree) deposit, Western Mongolia. Economic Geology 90, 530–547.
https://doi.org/10.2113/gsecongeo.90.3.530

Kynicky, J., Chakhmouradian, A.R., Xu, C., Krmicek, L. & Galiova, M., 2011. Distribution and evolution of zirconium mineralization in peralkaline granites and associated pegmatites of the Khan Bogd Complex, southern Mongolia. Canadian Mineralogist 49, 947–965. https://doi.org/10.3749/canmin.49.4.947

Lahti, I., Salmirinne, H., Kärenlampi, K. & Jylänki, J., 2018. Geophysical surveys and modelling of Nb–Zr–REE deposits and Fe–Ti–V ore-bearing gabbros in the Otanmäki area, central Finland. Geological Survey of Finland, Open File Work Report 75/2018, 30 p.

Lahtinen, R., Huhma, H., Lahaye, Y., Kousa, J. & Luukas, J., 2015. Archean–Proterozoic collision boundary in central Fennoscandia: Revisited. Precambrian Research 261, 127–165.
https://doi.org/10.1016/j.precamres.2015.02.012

Li, X.C. & Zhou, M.F., 2017. Hydrothermal alteration of monazite-(Ce) and chevkinite-(Ce) from the Sin Quyen Fe-Cu-LREE-Au deposit, northwestern Vietnam. American Mineralogist 102, 1525–1541.
https://doi.org/10.2138/am-2017-5970

Li, X.C. & Zhou, M.F., 2018. The nature and origin of hydrothermal REE mineralization in the Sin Quyen deposit, Northwestern Vietnam. Economic Geology 113, 645–673. https://doi.org/10.5382/econgeo.2018.4565

Liu, X., Dong, S., Xue, H. & Zhouy, J., 1999. Significance of allanite-(Ce) in granitic gneisses from the ultrahigh-pressure metamorphic terrane, Dabie Shan, central China. Mineralogical Magazine 63, 579–586.
https://doi.org/10.1180/002646199548628

Ludwig, K.R., 2008. Isoplot/Ex 3.70. A Geochronological Toolkit for Microsoft Excel. Berkeley Geochronological Center, Berkeley, Special Publication 4, 76 p.

Luth, R.W., 1988. Raman spectroscopic study of the solubility mechanisms of F in glasses in the system $CaO-CaF_2-SiO_2$. American Mineralogist 73, 297–305.

Marks, M., Venneman, T., Siebel, W. & Markl, G., 2003. Quantification of magmatic and hydrothermal processes in a peralkaline syenite–alkali granite complex based on textures, phase equilibria, and stable and radiogenic isotopes. Journal of Petrology 44, 1247–1280. https://doi.org/10.1093/petrology/44.7.1247

McDonald, R., Bagiński, B., Belkin, H.E. & Stachowicz, M., 2019. Composition, paragenesis, and alteration of the chevkinite-group of minerals. American Mineralogist 104, 348–369. https://doi.org/10.2138/am-2019-6772

McDonald, R., Bagiński, B., Kartashov, P., Zozulya, D. & Dzierżanowski, P., 2012. Chevkinite-group minerals from Russia and Mongolia: New compositional data from metasomatites and ore deposits. Mineralogical Magazine 76, 535–549. https://doi.org/10.1180/minmag.2012.076.3.06

McDonald, R., Bagiński, B., Kartashov, P.M., Zozulya, D., Dzierżanowski, P. & Jokubauskas, P., 2015. Hydrothermal alteration of a chevkinite-group mineral to a bastnäsite-(Ce)-ilmenite-columbite-(Fe): interaction with a F-, CO_2-rich fluid. Mineralogy and Petrology 109, 659–678. https://doi.org/10.1007/s00710-015-0394-2

McDonald, R., Belkin, H.E., Wall, F. & Bagiński, B., 2009. Compositional variation in the chevkinite group: new data from igneous and metamorphic rocks. Mineralogical Magazine 73, 777–796. https://doi.org/10.1180/minmag.2009.073.5.777

Middlemost, E.A.K., 1994. Naming materials in the magma/igneous rock system. Earth-Science Reviews 37, 215–224. https://doi.org/10.1016/0012-8252(94)90029-9

Morgenstern, R., Turnbull, R.E., Ashwell, P.A., Horton, T.W. & Oze, C., 2018. Petrological and geochemical characteristics of REE mineralization in the A-type French Creek Granite, New Zealand. Mineralium Deposita 54, 935–958. https://doi.org/10.1007/s00126-018-0854-9

Ni, H. & Keppler, H., 2013. Carbon in silicate melts. Reviews in Mineralogy & Geochemistry 75, 251–287. https://doi.org/10.2138/rmg.2013.75.9

Pan, L.C., Hu, R.Z., Bi, X.W., Li, C., Wang, X.S. & Zhu, J.J., 2018. Titanite major and trace element compositions as petrogenetic and metallogenic indicators of Mo ore deposits: examples from four granite plutons in the southern Yidun arc, SW China. American Mineralogist 103, 1417–1434. http://doi.org/10.2138/am-2018-6224

Papoutsa, A.D. & Pe-Piper, G., 2013. The relationship between REE-Y-Nb-Th minerals and the evolution of an A-type granite, Wentworth Pluton, Nova Scotia. American Mineralogist 98, 444–462. http://dx.doi.org/10.2138/am.2013.3972

Passchier, C.W. & Trouw, R.A.J., 2005. Microtectonics. 2nd ed., Springer-Verlag, Berlin, Heidelberg, New York, 366 p.

Petrik, I., Broska, I., Lipka, J. & Siman, P., 1995. Granitoid allanite-(Ce): Substitution relations, redox conditions and REE distributions (on an example of I-type granitoids, Western Carpathians, Slovakia). Geologica Carpathica 46, 79–94.

Rasilainen, K., Lahtinen, R. & Bornhorst, T.J., 2007. The Rock Geochemical Database of Finland Manual. Geological Survey of Finland, Report of Investigation 164, 38 p.

Rudnick, R.L. & Gao, S., 2003. Composition of the continental crust. In: Rudnick, R.L. (ed.), The Crust. Treatise on Geochemistry, Volume 3. Elsevier-Pergamon, Oxford, pp. 1–64.

Salvi, S. & Williams-Jones, A.E., 2005. Alkaline granite-syenite deposits. In: Linnen, R.L., Samson, I.M. (eds.), Rare Element Geochemistry and Mineral Deposits. Geological Association of Canada, Short Course Notes 17, 315–341.

Sarapää, O., Al-Ani ,T., Lahti, S.I., Sarala, P., Torppa, A. & Kontinen, A., 2013. Rare earth exploration potential in Finland. Journal of Geochemical Exploration 133, 25–41. https://doi.org/10.1016/j.gexplo.2013.05.003

Sarapää, O., Kärkkäinen, N., Ahtola, T. & Al-Ani, T., 2015. High-tech metals in Finland. In: Maier, W., O'Brien, H., Lahtinen, R. (eds.), Mineral Deposits of Finland. Elsevier, Amsterdam, pp. 613–632. https://doi.org/10.1016/B978-0-12-410438-9.00023-6

Savel'eva V.B. & Karmanov, N.S., 2008. REE minerals of alkaline metasomatic rocks in the Main Sayan Fault. Geology of Ore Deposits 50, 681–696. https://doi.org/10.1134/S1075701508080035

Schmitt, A.K., Trumbull, R.B., Dulski, P. & Emmermann, R., 2002. Zr-Nb-REE mineralization in peralkaline granite from the Amis Complex, Brandberg (Namibia): evidence for magmatic pre-enrichment from melt inclusions. Economic Geology 97, 399–413. https://doi.org/10.2113/gsecongeo.97.2.399

Shand, S.J., 1943. Eruptive Rocks. Their Genesis Composition, Classification, and Their Relation to Ore-Deposits with a Chapter on Meteorites. John Wiley & Sons, New York, 444 p.

Shellnut, J.G., Wang, K.L., Zellmer, G.F., Iizuka, Y., Jahn, B.M., Pang, K.N., Qi, L. & Zhou, M.F., 2011. Three Fe-Ti oxide ore bearing gabbro-granitoid complexes in the Panxi region of the Permian Emeishan large igneous province, SW China. American Journal of Science 311, 773–812. https://doi.org/10.2475/09.2011.02

Shu, X. & Liu Y., 2019. Fluid inclusion constraints on the hydrothermal evolution of the Dalucao Carbonatite-related REE deposit, Sichuan Province, China. Ore Geology Reviews 107, 41–57. https://doi.org/10.1016/j.oregeorev.2019.02.014

Siegel, K., Vasyukova, O.V. & Williams-Jones, A.E., 2018. Magmatic evolution and controls on rare metal-enrichment of the Strange Lake A-type peralkaline granitic pluton, Québec-Labrador. Lithos 308–309, 34–52. https://doi.org/10.1016/j.lithos.2018.03.003

Spicer, E.M., 2001. Apatite, allanite, titanite and monazite characteristics in S-, I- and A-type Cape Granites. MSc Thesis, University of Stellenbosch, 107 p.

Stebbins, J.F. & Zeng, Q., 2000. Cation ordering at fluoride sites in silicate glasses: a high-resolution ^{19}F NMR study. Journal of Non-Crystalline Solids 262, 1–5. https://doi.org/10.1016/S0022-3093(99)00695-X

Sun, S.-S. & McDonough, W.F., 1989. Chemical and isotopic systematics of oceanic basalts: implications for mantle composition and processes. Geological Society of London, Special Publication 42, 313–345. https://doi.org/10.1144/GSL.SP.1989.042.01.19

Sun, Y., Lai, Y., Chen, J., Shu, Q. & Yan, C., 2013. Rare earth and rare metal elements mobility and mineralization during magmatic and fluid evolution in alkaline granite system: evidence from fluid and melt inclusions in Baerzhe granite, China. Resource Geology 63, 239–261. https://doi.org/10.1111/rge.12007

USGS, 2020. Mineral commodity summaries 2020. U.S. Geological Survey, 200 p.

Vasyukova, O. & Williams-Jones, A.E., 2014. Fluoride-silicate melt immiscibility and its roles in REE ore formation: evidence from the Strange Lake rare metal deposit, Québec-Labrador, Canada. Geochimica et Cosmochimica Acta 139, 110–130. http://dx.doi.org/10.1016/j.gca.2014.04.031

Verbaan, N., Bradley, K., Brown, J. & Mackie, S., 2015. A review of hydrometallurgical flowsheets considered in current REE projects. In: Simandl, G.J. and Neetz, M. (eds.), Symposium on Strategic and Critical Materials Proceedings, November 13-14, 2015, Victoria, British Columbia. British Columbia Ministry of Energy and Mines, British Columbia Geological Survey Paper 2015-3, pp. 147–162.

Vilalva, F.C.J, Vlach, S.R.F. & Simonetti, A., 2016. Chemical and O-isotope compositions of amphiboles and clinopyroxenes from A-type granites of the Papanduva Pluton, South Brazil: Insights into late- to post-magmatic evolution of peralkaline systems. Chemical Geology 420, 186–199. https://doi.org/10.1016/j.chemgeo.2015.11.019

Vlach, S.R.F. & Gualda, G.A.R., 2007. Allanite and chevkinite in A-type granites and syenites of the Graciosa Province, southern Brazil. Lithos 97, 98–121. https://doi.org/10.1016/j.lithos.2006.12.003

Vuorinen, J.H. & Hålenius, U., 2005. Nb-, Zr- and LREE-rich titanite from the Alnö alkaline complex: crystal chemistry and its importance as a petrogenetic indicator. Lithos 83, 128–142. https://doi.org/10.1016/j.lithos.2005.01.008

Watanabe, Y., Kon, Y., Echigo, T. & Kamei, A., 2016. Differential fractionation of rare earth elements in oxidized and reduced granitic rocks: implication for heavy rare earth enriched ion adsorption mineralization. Resource Geology 67, 35–52. https://doi.org/10.1111/rge.12119

Weng, Z., Jowitt, S.M., Mudd, G.M. & Haque, N., 2015. A detailed assessment of global rare earth element resources: opportunities and challenges. Economic Geology 110, 1925–1952. https://doi.org/10.2113/econgeo.110.8.1925

Wones, D.R., 1989. Significance of the assemblage titanite+magnetite+quartz in granitic rocks. American Mineralogist 74, 744–749.

Zheng, X. & Liu, Y., 2019. Mechanisms of element precipitation in carbonatite-related rare-earth element deposits: Evidence from fluid inclusions in the Maoniuping deposit, Sichuan Province, southwestern China. Ore Geology Reviews 107, 218–238. https://doi.org/10.1016/j.oregeorev.2019.02.021

Zimova, M. & Webb, S.L., 2007. The combined effects of chlorine and fluorine on the viscosity of aluminosilicate melts. Geochimica et Cosmochimica Acta 71, 1553–1562. https://doi.org/10.1016/j.gca.2006.12.002

Zozulya, D., Kullerud, K., Ravna, E.K., Corfu, F. & Savchenko Y., 2009. Geology, age and geochemical constraints on the origin of the Late Archean Mikkelvik alkaline stock, West Troms Basement Complex in Northern Norway. Norwegian Journal of Geology 89, 327–340.